ASM Handbook, Volume 24, *Additive Manufacturing Processes*
D. Bourell, W. Frazier, H. Kuhn, M. Seifi, editors
DOI 10.31399/asm.hb.v24.a0006578

Vat-Photopolymerization-Based Ceramic Manufacturing

Xiangjia Li and Yong Chen, University of Southern California

CERAMICS are one type of inorganic and nonmetallic material, and their crystalline structure and chemical composition result in excellent physical properties, including mechanical, thermal, chemical, optical, electrical, and magnetic properties (Ref 1). Due to these versatile properties, ceramics are widely used in many different applications, such as thermal-protection shields in aerospace, bioimplants in biomedical engineering, pump filters and catalysts in the chemical industry, sensors and dielectrics in electronics, and cutting tools in manufacturing (Fig. 1) (Ref 1). With the increasing use of ceramics in different fields, various forming methods were developed over the last 100 years. However, with conventional manufacturing techniques, such as injection molding, die pressing, tape casting, throwing, and so on, it is difficult to satisfy the processing demand of ceramic parts with complex geometric design due to the limited fabrication capability (Ref 2). For example, bioceramic-based scaffold is customized based on the shape of the defect, and it is filled with interconnected holes, making it impossible to be built using the aforementioned manufacturing techniques (Ref 2). In the last 30 years, the manufacturing community has benefited from additive manufacturing (AM), also known as three-dimensional (3D) printing, which enables the fabrication of a 3D object from scratch using a wide range of materials (Ref 3). Additive manufacturing shows excellent advantages in building 3D objects with complex geometry, and this unique manufacturing method makes it possible to fabricate customized ceramic structure with high accuracy that is difficult for conventional manufacturing techniques (Ref 4). Several ceramic AM processes, including vat photopolymerization (VPP), two-photon polymerization (TPP), fused-deposition modeling (FDM), direct ink writing (DIW), inkjet printing, powder binder jetting, selective laser sintering/melting (SLS/M), and laminated object manufacturing, have been developed (Fig. 1) (Ref 5, 6). With the development of ceramic 3D printing, different types of ceramics may be fabricated to study their chemical, electrical, optical, thermal, and mechanical functionalities, giving designers and engineers more flexibility to be innovative without being limited by traditional manufacturing methods (Ref 5, 6).

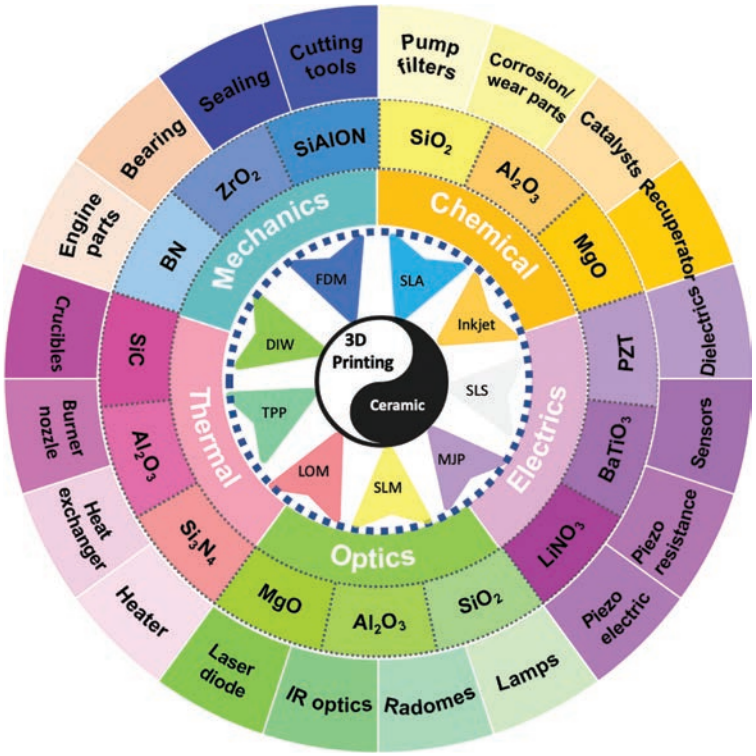

Fig. 1 Current additive manufacturing processes developed to fabricate ceramic components. IR, infrared; PZT, lead zirconate titanate; SLA, stereolithography; SLS, selective laser sintering; MJP, multijet printing; SLM, selective laser melting; LOM, laminated object manufacturing; TPP, two-photon polymerization; DIW, direct ink writing; FDM, fused-deposition modeling

According to the physical phase of the printing material, ceramic AM processes can be broadly divided into two main categories: powder-based ceramic printing and slurry-based ceramic printing (Ref 2). In powder-based ceramic printing, ceramic powder is first spread by a paving mechanism on the powder bed, and the printing process, after the ceramic powder is spread, varies in principle. Major powder-based ceramic printing processes are inkjet printing (Ref 7), binder jetting (Ref 8), and SLS/M (Ref 9). For example, binder jetting is a technology in which binder is selectively deposited over the spread ceramic powder layer, and, with the help of binder, the ceramic powder is accumulated layer by layer to form a 3D shape (Fig. 2) (Ref 8). For binder jetting, postprocesses that include postcuring, depowdering, sintering, infiltration, annealing, and finishing are necessary to obtain high-quality ceramic parts (Ref 5). Because solid

powder plays the role of support, binder jetting exhibits strength for fabricating components that have complex inner structures, and the process is widely used in the fabrication of bioceramic-based scaffolds for tissue engineering (Ref 8). Without adding extra binder, SLS is widely used to fabricate powder-based material, such as metal, ceramics, and plastics (Ref 9). In SLS, a high-power laser beam is used to irradiate the selected ceramic powder, and the targeted powders will be heated up and sintered to the bulk joining point (Ref 9). Unlike binder jetting, which requires postprocessing to remove the binder, SLS can directly obtain the 3D-printed ceramic part without postprocessing. In general, powder-based ceramic 3D printing shows advantages in the fabrication of parts with complex cellular structures (Ref 2, 7–9).

In slurry-based ceramic printing, high-viscous slurry composed of ceramic particles and other liquids is deposited in a layer-by-layer manner to form a 3D object (Ref 2). For example, in FDM-based ceramic printing, a filament is fed and heated to a molten or semimolten state. The melted slurry extruded from the nozzle under the pressure of a piston will deposit and fuse with the adjacent part that has already been deposited (Ref 10, 11). However, it is difficult to directly shape ceramics into filaments, due to their brittle mechanical property. Therefore, to use FDM to fabricate ceramic components, the ceramic particles are mixed with thermoplastic binders to form filament feedstock (Fig. 2) (Ref 12). After finishing the printing process, debinding and sintering must be conducted to accomplish binder removal and densification (Ref 11, 12). Ceramic transducers (Ref 12) and bioceramic-based scaffolds (Ref 13–16) with lattice structures having spatial resolutions smaller than 100 μm can be fabricated by using FDM-based ceramic printing. Ceramic-based slurry can also be fabricated by using DIW, in which an ink-deposition nozzle is used to deposit the slurry to generate the 3D architecture and composition (Fig. 2) (Ref 17). Compared with other ceramic 3D printing processes, DIW is a cheap and fast manufacturing process that has the capability of fabricating numerous different structures, ranging from solid monolithic parts (Ref 18) to complex porous scaffolds (Ref 19). However, the density of a ceramic part fabricated by the DIW process is not as high as that of the powder-based approaches. This is because the viscosity of ink goes up dramatically with the increase in ceramic particle concentration, and the high-viscous slurry is hard to extrude from the ink-deposition nozzle. In addition, the ceramic particle size should be much smaller than the nozzle tip; otherwise, the ceramic particles will easily block the nozzle tip (Ref 17).

Most of the slurry-based ceramic fabrication using 3D printing in modern times has evolved to be a combination of AM and heat-treatment-based consolidation (Ref 2). Such a process begins with green-part fabrication of a ceramic-polymer composite by using various types of 3D printing processes, such as FDM (Ref 13–15), DIW (Ref 17–19), TPP (Ref 2), and VPP (Ref 9). A heat treatment procedure, including debinding and sintering, is necessary to form the consolidated part (Ref 2). The ceramic-polymer composite is also constantly investigated to find the best degree of manufacturability, where the viscosity of the slurry is adjusted to provide a sufficient density of the ceramic ingredient within the mixture (Ref 2, 4).

Vat Photopolymerization

The AM revolution has brought new possibilities in designing and building objects with complex freeform surfaces (Ref 20, 21). Various AM processes were developed to overcome the difficulty of traditional manufacturing in terms of 3D fabrication, and a large range of materials, including difficult-to-process material, can now be formed into 3D shapes using AM technologies (Ref 22, 23). Due to its advantages, AM technologies have been widely used in every area of social life, such as aerospace, biomedical engineering, civil engineering, electronics, and so on (Ref 20, 21). Among all the AM processes, VPP shows unique capability and demonstrates superiority in a wide variety of applications (Ref 24, 25). Vat photopolymerization was developed based on one type of chemical reaction, called photopolymerization, in which the photocurable polymer is cross linked by the initiation of light exposure (Ref 23). The material phase transforms from liquid to solid, forming a linear or cross-linked polymer structure in the photopolymerization process (Ref 23). In VPP, a vat of liquid resin, which is composed of monomers, oligomers, and photoinitiators, undergoes the aforementioned chemical reaction and selectively accumulates into a 3D shape defined by the exposed ultraviolet (UV) light (Ref 23).

Various VPP processes have been developed to improve printing capability, including laser writing stereolithography (LWSL) (Ref 26), mask-image-projection-based stereolithography (MIP-SL) (Ref 27–31), continuous light interface process (Ref 32), physical-field-assisted-stereolithography (Ref 33), and TPP (Ref 34). In LWSL, a laser beam with controllable power and wavelength is reflected by high-speed-scanning galvo mirrors and is further focused on the surface of the liquid resin (Ref 26). Following the generated tool path, the laser beam solidifies the liquid polymer into a special two-dimensional (2D) pattern. After that, the platform moves down a distance of one layer thickness, and liquid resin fills back to the fabrication area to facilitate the fabrication of the next layer (Ref 23). To achieve multiscale fabrication, the laser beam size can be dynamically adjusted based on the geometric shape of the printed object

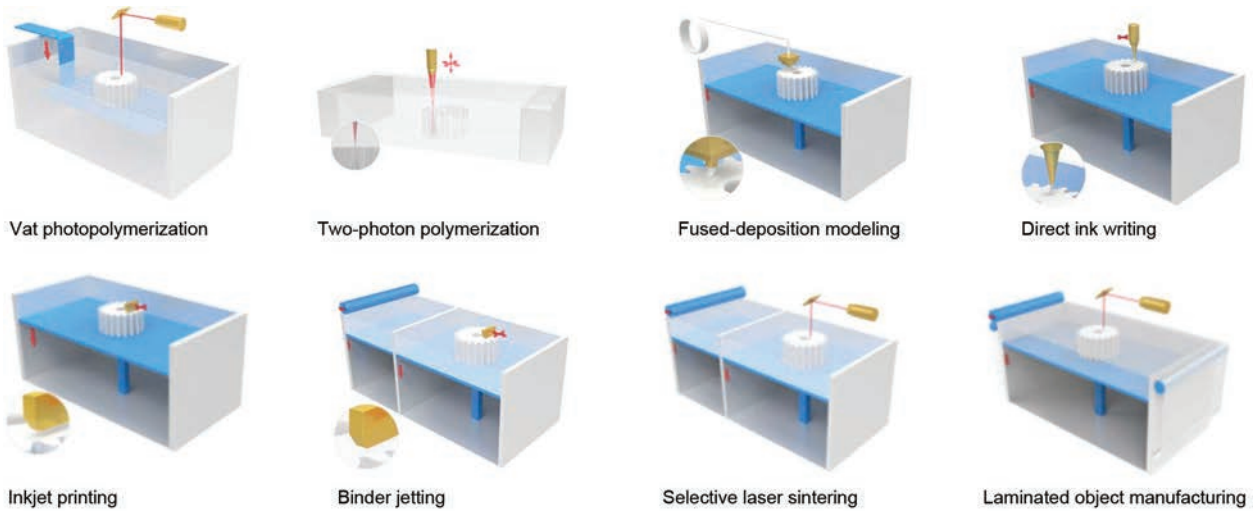

Fig. 2 Current additive manufacturing processes developed to fabricate ceramic components. Source: Ref 2

(Ref 26). In MIP-SL, a digital micromirror device is used to generate a 2D-patterned light beam, and the whole layer of resin can be cured with only a single exposure (Ref 23, 32, 33). Based on the oxygen-inhibition layer and two-way movements, centimeters-tall objects can be printed within several minutes, which is 100 times faster than other AM approaches (Ref 30, 31). In TPP, an ultrafast laser beam is used to irradiate the photopolymer, which requires much high energy to be cross linked (Ref 34, 35). Because TPP is a volume-based 3D printing process, there is no topological constraint, and complex 3D shapes with submicrometer features can be directly printed using TPP (Ref 35). Due to its unique capability, TPP has been applied to many applications, such as micro/nanophotonics, microelectromechanical systems, microfluidics, biomedical implants, and microscale devices (Ref 34).

A large range of materials, including plastics (Ref 36), ceramics (Ref 2), metals (Ref 37), and composite materials (Ref 38), are used in VPP. When using VPP to fabricate noncurable materials, a mixture composed of both noncurable material and photopolymer is formed into 3D shape during photopolymerization of the photocurable polymer (Ref 2, 32, 37). For example, a nanoscale graphene platelet based composite material was formed into nacre-inspired structures by using electrically assisted MIP-SL, and the printed material showed mechanical reinforcement and electrical self-sensing capabilities (Ref 32). To obtain pure noncurable material, the photopolymer in the fabricated object can be removed by postprocessing methods, such as chemical dissolution (Ref 39), thermal decomposition (Ref 3), or microwave sintering (Ref 40). For example, both pure metallic and ceramic microscale lattices, which were extraordinary light and stiff, were fabricated by using microscale MIP-SL. After the printing process, thermal decomposition and sintering were applied to remove the polymer and to densify the metallic and ceramic (Ref 39). Similarly, 3D-shaped fused silica glass designed with complex inner structures was obtained after debinding and sintering the polymerized composite fabricated by the VPP process (Ref 41). Due to its unique strengths, such as high detail accuracy (Ref 29), geometric complexity (Ref 39), smooth surface quality (Ref 25, 42), large materials selection (Ref 32, 33, 36, 37), and fast speed (Ref 27, 30, 31), VPP is one of the more popular 3D printing techniques (Ref 43, 44).

Vat-Photopolymerization-Based Ceramic Fabrication

Similar to polymers, a ceramic part can be fabricated by the VPP-based 3D printing process with high resolution and surface quality (Ref 45). The procedure of ceramic fabrication by using the VPP process is shown in Fig. 3. First, the microscale or nanoscale ceramic particles are mixed with the photocurable resin; then, using the slurry mixture, the green part is prepared by VPP-based ceramic printing (Ref 3). In the VPP-based ceramic printing process, the photopolymer mixed with the ceramic particles undergoes a chemical reaction (photopolymerization) and further forms a solid part defined by the radiation light in the UV range of wavelengths (Ref 45). After that, general postprocessing, including low-temperature debinding and high-temperature sintering, is necessary to remove the inner polymer and fuse the ceramic particles together (Ref 3). Information and methods of material preparation, green-part fabrication, postprocessing, property identification, and polymer-derived ceramics are introduced in this section.

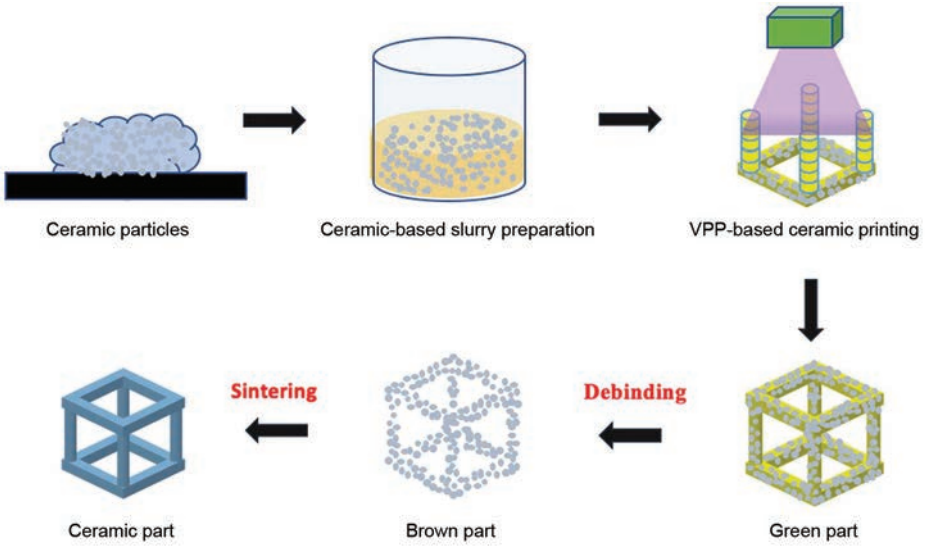

Fig. 3 Flowchart of vat photopolymerization (VPP)-based ceramic fabrication

Material Preparation

To print ceramic components using the VPP-based 3D printing process, a ceramic composite slurry is prepared by mixing ceramic filler particles with photocurable resin (Ref 45). During the fabrication process, the slurry is selectively cured by light exposure, and the resin serves as a binder to bond ceramic particles into the desired 3D shape (Ref 3). As the first step, the preparation of the slurry is critical to the whole fabrication process. Specifically, the ceramic powder must be nonagglomerating in an azeotropic mixture, with the dispersant added by ball milling to obtain a homogeneous distribution (Ref 3). Often, the dispersant can simply be added to the monomer solution. Figure 4(a) shows a flowchart for slurry preparation. After evaporation of the solvent, the dried ceramic particles with dispersant adsorbed onto their surface will be mixed with a photocurable resin. Then, the premixed resin and ceramic particles go through the ball-milling process again until the mixture becomes a homogeneous slurry (Ref 3).

Homogeneity of the slurry, which determines the quality of a 3D-printed part, is an important factor that must be considered during the manufacturing process. The inhomogeneity of ceramic particles in the slurry caused by sedimentation, which results from the aggregation of ceramic particles, will generate defects in the final ceramic part after removing the polymer (Fig. 4b) (Ref 3). To control the slurry homogeneity, one must understand the slurry-preparation mechanism. The slurry is a mixture of ceramic particles and photocurable resin. These micro- or nanoscale ceramic particles inside the slurry are extremely easy to aggregate due to van der Waals attractive forces (Ref 3). Due to particle aggregation, the inhomogeneity of the slurry causes nonisotropic distribution of ceramic particles inside the final green part (Ref 3). Hence, defects and failure, such as cracking and delamination, may occur during postprocessing due to the nonuniform stress inside the green part, caused by the inhomogeneous distribution of ceramic particles (Fig. 4b) (Ref 3). To eliminate this problem, the ceramic-based slurry should be prepared according to the procedures discussed previously.

Curing Characteristics

After the slurry is prepared, the curing performance of the ceramic slurry should be studied to obtain the best fabrication parameter values. Compared to the pure photocurable resin, the curing characteristics of the ceramic composite slurry are quite different (Ref 46). When light travels through the slurry, the direction of the light will be changed due to the scattering effect of the ceramic particles inside the ceramic slurry (Ref 47). Therefore, the

penetration depth of the light and the curing depth for the slurry are dramatically decreased. Based on a study (Ref 3), the cure depth for ceramic composite slurry is mainly affected by the resin sensitivity and the ceramic refractive index. The penetration depth of light, D_p, can be determined by (Ref 3):

$$\frac{1}{D_p} = \varepsilon_P c_P + \varepsilon_D c_D + (\beta - \varepsilon_P c_P + \varepsilon_D c_D)\phi - \left(\frac{\beta}{2\phi_{max}}\right)\phi^2 \quad \text{(Eq 1)}$$

where ε_P and ε_D are molar extinction coefficients of the photoinitiator and dye, respectively; c_P and c_D are the concentrations in volume unit of photoinitiator and dye in the slurry, respectively; β is the variation in scattering, determined by the refractive index contrast; ϕ is the volume fraction of ceramic particles; and ϕ_{max} is the maximum concentration of ceramic inside the slurry.

Overall, the cure depth of the slurry is determined by the refractive index difference between the filler ceramic particles and the photocurable resin, the particle size, and the solid loading of ceramic particles in the slurry (Ref 3, 46). After the cure depth is decided, the layer thickness should be smaller than the cure depth of slurry, so that the newly cured layer can be attached on the surface of the previously cured layers.

Green-Part Fabrication

The viscosity of the ceramic composite slurry is dramatically increased with the increment of ceramic particles concentration. To fabricate by using the layer-by-layer approach, the rheological characteristic of the ceramic slurry should be studied in the VPP-based ceramic printing process (Ref 48). Due to relatively low viscosity and good flowability, the pure photocurable resin is able to refill small gaps by itself in the normal VPP process (Ref 49). However, because of its poor flowability, the ceramic composite slurry with high viscosity cannot self-refill a gap if driven only by air pressure and self-gravity (Ref 48). To solve the filling problem, a doctor-blade-based material feeding system, which can recoat a thin layer of slurry with desirable thickness, was introduced in the VPP-based ceramic printing process (Ref 3, 49). The basic design of a VPP-based ceramic fabrication machine is shown in Fig. 5(a). To fabricate the green

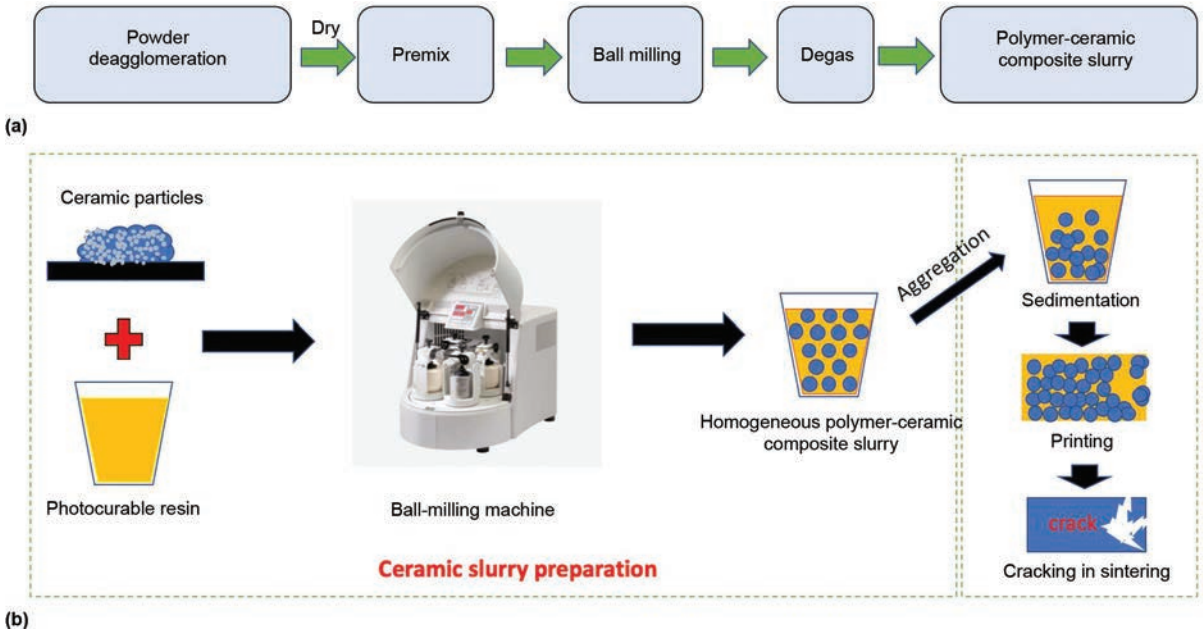

Fig. 4 Material preparation in vat-photopolymerization-based ceramic fabrication. (a) Flowchart of slurry-preparation procedure. (b) Homogeneity problem in slurry fabrication

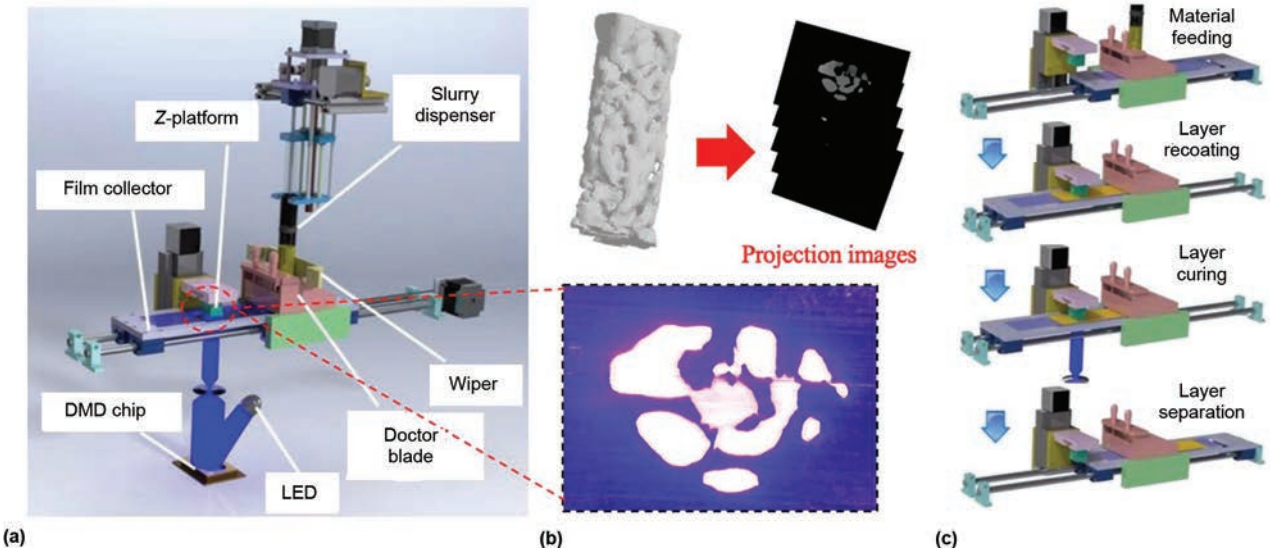

Fig. 5 Green-part fabrication by using the vat photopolymerization (VPP)-based ceramic printing process. (a) Diagram of VPP-based ceramic printing. DMD, digital micromirror device; LED, light-emitting diode. (b) Set of projection images generated by slicing the digital model in VPP-based ceramic printing. (c) Process planning of green-part fabrication by using the VPP-based ceramic printing process

part, a series of 2D mask images are generated by slicing the digital model of the building part (Fig. 5b) (Ref 3). The projection light defined by each mask image is exposed on the surface of the recoated slurry in sequence. After one layer is cured solid, a small amount of slurry is fed, and a uniform layer of slurry will be recoated on the glass plate by the doctor blade. After that, the light coming from the bottom will project onto the surface of the slurry, and a new layer of ceramic will solidify and attach onto the surface of the precured layers (Fig. 5c). By repeating the process layer by layer, a green part with desired 3D shape is formed by VPP-based ceramic printing.

Process Design and Planning

Because the properties of the slurry significantly influence the performance of the VPP-based ceramic printing process, the relationship between material properties and process parameters must be studied in order to set process parameters to successfully build a ceramic component (Ref 3). For each layer, a small amount of slurry is deposited on the fabrication surface behind the doctor blade; then, the blade pushes the slurry to form a thin layer of material with desirable thickness. However, to achieve the desired thickness, several process parameters, including gap distance between the blade and the synthetic fluorine-containing resin film, the moving speed of the film collector, and others, must be considered (Fig. 6b). Because the pressure in the dispensed slurry can be ignored, the blade recoating procedure can be modeled with a plane Couette flow pattern (Ref 48, 50). As shown in Fig. 6(b), the bottom plate moves at a constant speed of V_r relative to the blade. To generate the uniform thickness, d, of a slurry layer, the gap, g_{blade}, of the blade should be:

$$g_{blade} > \frac{2\alpha\rho' d}{r\rho} \quad \text{(Eq 2)}$$

where ρ is the slurry density, and ρ' is the density of the newly formed layer, and r is the width ratio of the slurry layer before and after recoating. To ensure layer bonding, α is a safety factor to ensure that neighboring layers will be bonded ($\alpha > 1$).

When the ceramic slurry passes the doctor blade, it has a lower viscosity, caused by a higher shear rate due to the shear thinning behavior of the ceramic slurry (Ref 3). Thus, sedimentation of ceramic particles in the recoated layer can be avoided, and good homogeneity of the fabricated green parts can be achieved (Ref 3). With the same blade gap, g, a higher recoating speed, V_r, or a larger slurry viscosity will generate a bigger shear rate, γ (Ref 48).

In the printing process, the platform goes up a small distance (smaller than the cure depth of the slurry) from the fabrication surface after the fabrication of each layer. Then, the film collector moves in the x-axis with a speed, V_r, to detach the newly cured layer from the fabrication surface, and a new layer of slurry is coated at a thickness of δ' (Ref 48). As shown in Fig. 5(c), when the part slides from left to right, the portion of the cylinder immersed in the slurry layer experiences a drag force, F, in the slurry moving direction as the average force, q ($q = F/\delta'$) (Ref 3). Suppose a cylindrical shape is being fabricated whose diameter is D and the current building height is L. The sliding speed of V_r should be set in the range shown in Eq 3 to avoid damage to the printed features:

$$0 < V_r < \sqrt{\frac{[\sigma]D^2}{8\rho C_D \delta' L}} \quad \text{(Eq 3)}$$

where σ is the bending stress of the cured material; ρ is the mass density of the slurry; and C_D is the drag coefficient, which is related to the Reynolds number, Re, of the slurry and can be identified by experiments.

The conventional material recoating method is shown in Fig. 5(c); the film collector must move from left to right for layer recoating and then move from right to left for the generation of a new layer. This method spends more time on the motion of the film collector (Ref 3). A fast recoating method was developed to reduce the motion time and to speed up the material feeding process in the VPP-based printing process (Fig. 6a) (Ref 33). In this continuous feeding process, the film collector was designed to be a circular plate, which was mounted on the rotary stage, and the layer recoating can be achieved by rotation the plate (Ref 33).

The slurry was continuously extruded from the gap generated by the doctor blade and spread to a thin film during the continuous rotation in one direction (Ref 33).

Support Development

To fabricate ceramics with complex inner structures such as overhangs, supports must be designed and fabricated with the structure. However, a support brings many problems to the 3D printing of a single material (Ref 1). For example, it is very difficult to remove supports without causing extra damage to parts with delicate features. To overcome these challenges, many research activities have been done to optimize support generation in the VPP-based ceramic printing process. New

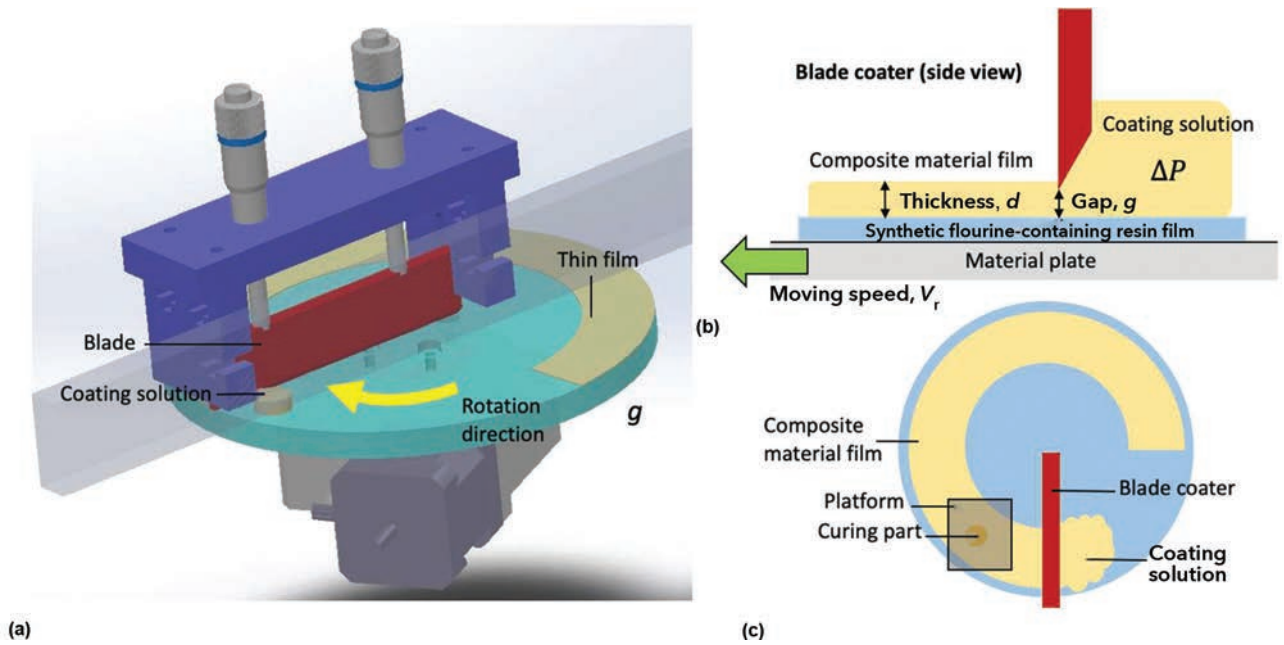

Fig. 6 Material recoating process in the vat-photopolymerization-based ceramic printing process. (a) Slurry recoating process based on rotation. (b) Side view of slurry recoating. (c) Top view of slurry recoating

methods for support detection were developed for the VPP process in the past decades. For example, a surface element (surfel) convolutional neural-network-based approach was developed to reduce the number of supports and increase the accuracy of the support position during support detection (Ref 51). This method produced a local surfel image, which contained the local topology information of the sampling point defined by the layered depth-normal image, and a set of models with ground-truth support regions were used to train the deep neural network (Ref 51). In addition, researchers have studied some novel approaches to developing a highly removable support structure for the fabrication process. Researchers used solid ice as the support material, which can be easily removed after fabrication without causing any damage to the component surface (Ref 52). During the 3D printing process, a cooling device was used to freeze water, and then the photocurable resin that is spread on the ice surface is solidified by projection light (Ref 52). Both approaches can be applied to VPP-based ceramic fabrication for support generation.

Furthermore, some support-free fabrication methods have been developed to improve the quality of 3D-printed green parts. A high-yield-stress ceramic slurry was used as the feedstock material, which exploits the elastic force of the material to support overhanging features without the need to build additional support structures (Ref 53). Based on that, Song et al. developed a new ceramic stereolithography (CSL) method that avoids the need for additional support (Ref 54). In this CSL-based approach, an elastoviscoplastic ceramic suspension that has inherently strong interparticle force was used as a support bed, so that an additional support structure is not necessary when fabricating a part with overhang features (Fig. 7) (Ref 54).

Quality Control and Optimization

To achieve high quality and reproducibility, it is important to have quality control in the VPP-based ceramic printing process. In addition, due to the complexity of the printing and postprocessing processes, the optimization of process parameters is also indispensable. Many research studies have been conducted to study quality control and optimization in VPP. For example, Xu et al. studied part-fabrication mechanisms and determined that three most significant sources, such as over- or underexposure, light blurring, and phase change, induced shrinkage or expansion of the part printed by the VPP process (Ref 55). Zhou et al. increased the printing accuracy of the VPP process by optimizing process parameters (Ref 56). By measuring the printed part quality, the manufacturing process parameters, including layer thickness, resultant overcure, hatch space, blade gap, and part location, were optimized to improve the printing quality (Ref 56). Polymerization shrinkage and thermal cooling effect are two major factors that lead to curl distortion in the VPP process. Kai et al. studied the photocuring temperature during the MIP-SL process by using a high-resolution infrared camera. After the experimental study, they discovered the temperature distribution during the printing process and further developed some new exposure strategies that can effectively reduce curl distortion (Ref 57). Based on these previous studies, the process parameters of VPP-based ceramic printing can be further optimized to achieve better quality control.

Postprocessing

Debinding

The debinding process is aimed at thoroughly removing the polymer ingredient, which is used as the binder in the material mixture in order to form the desired part geometry in the VPP-based ceramic printing process (Fig. 8a) (Ref 58). Particularly, the photocurable polymer is mixed with the desired ceramic particles and cured to the intended shape, which is called the green part, under a projected light or laser (Ref 3). Subsequently, the debinding process is conducted on the green part to pyrolyze the polymer inside through a controlled process of raising the temperature to 600 °C (1110 °F) in a furnace environment (Ref 59). The green part is initially heated from room temperature, followed by a process of slowly ramping up the temperature to prevent heat-formed cracking (Ref 59). At a certain threshold temperature, the value is held for a certain amount of time to heat the part thoroughly before the temperature is again raised to a higher stage. For example, barium titanate (BTO) is heated at a rate of 1 °C/min (1.8 °F/min), with incremental pauses for 30 min at temperature thresholds of 200, 300, 400, and 500 °C (390, 570, 750, 930 °F), respectively. The temperature eventually reaches and is maintained at 600 °C, upon which the polymer continues to pyrolyze for 3 h toward full vaporization (Fig. 8d) (Ref 60).

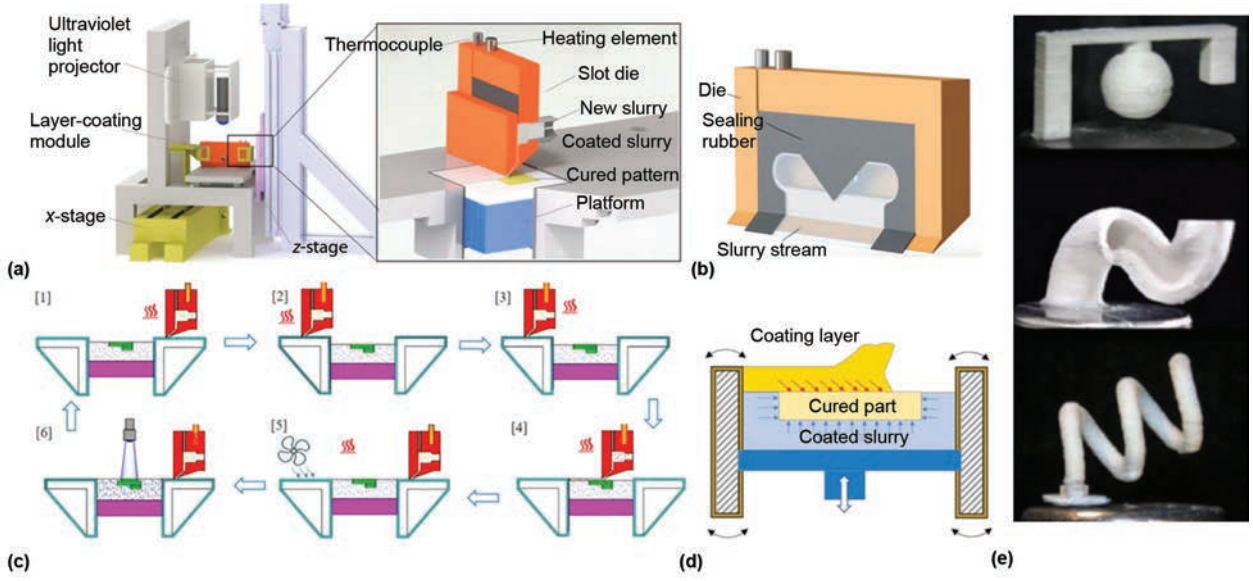

Fig. 7 No-support ceramic fabrication by the vat-photopolymerization-based ceramic printing process. (a–b) Schematic diagram of suspension-enclosing projection stereolithography. (c) Procedure for one-layer fabrication. (d) Supporting mechanism for overhang feature fabrication. (e) Three-dimensional-printed ceramic parts without added supports. Source: Ref 54

Currently, major debinding approaches are mainly categorized into thermal- (Ref 59), solvent- (Ref 61), and microwave- (Ref 62) based methods (Ref 3). In thermal-based debinding methods, vacuum debinding eliminates damage caused by oxidization of the materials and features a reduced cycle time for the process (Ref 60). Typically, debinding is done in air. The choice of debinding atmosphere is often determined by the powder. Inert-gas-based debinding can have a similar effect as the vacuum debinding process. Gases, such as argon and nitrogen, are applied in the debinding environment to prevent oxidization and the corresponding damage to the fragile green part. In both vacuum- and inert-gas-based debinding processes, a vital process specification is evacuation of the vaporized polymer (Ref 60). For solid parts at relatively large scale, the vaporized polymer is prone to be trapped inside the object, causing defective parts with cracks, notches, and unpredictable fractures, whereas a part with a thin-wall feature, interconnected and porous structure, or simply smaller scale of dimension would have a superior performance with respect to gas evacuation of the vaporized polymer. In practice, vaporized and evacuated polymers would turn into carbon, which, in turn, attaches to the surface of a part, blackening the part in high temperature while leaving pores in the meantime (Fig. 8b).

Sintering

By definition, the sintering process of ceramic is to fuse the ceramic particles together to fill the porosity left by pyrolyzed polymer (Fig. 8c). There are two major approaches currently being adopted: thermal- and microwave-based sintering processes (Ref 40, 60). Thermal-based sintering is normally a process that heats the part from more than 1000 °C (1830 °F) to achieve grain growth. Similar to the debinding process, the procedure begins with heating the part from room temperature, followed by faster temperature increments usually at a rate that is higher than the one used in the debinding process. Similarly, the temperature is then held at certain levels to heat the part thoroughly; eventually, it is raised to and kept at a sufficient level for grain growth to take place. The highest sintering temperature and the time needed are determined by the ceramic material to be fabricated (Ref 63). As an example, hydroxyapatite/tricalcium phosphate (HA/TCP) is heated at a rate of 3 °C/min (5.4 °F/min), and the temperature is held for 30 min, respectively, at 200, 300, 600, 1000, and 1100 °C (390, 570, 1110, 1830, and 2010 °F), with the last temperature step being kept at 1250 °C (2280 °F) for 3 h (Fig. 8d). In comparison, BTO exhibits a different heating curve than HA/TCP, with a higher temperature of 1330 °C (2425 °F) being held for 6 h for the final sintering step (Ref 60).

The microwave sintering process, compared with the thermal sintering process, is of higher power at the same level of energy consumption (Ref 40). Microwave energy penetrates the green part, is absorbed by the matter, and is uniformly transformed into heat inside the part, while thermal sintering must inefficiently transport heat from outside to inside (Ref 40). As a result, microwave sintering requires less sintering time and has controllable grain growth, which leads to less porosity and higher densification. The major drawback of microwave sintering, however, is the cost and the equipment capability in handling different scales of parts (Ref 63). The equipment of microwave sintering is relatively more expensive than that of thermal sintering and is usually restricted in size capability, which would be a significant limitation in some dimensionally focused cases.

Shrinkage and Compensation

The phenomenon of shrinkage is inevitably associated with the removal of polymer in the debinding process and the densification in the sintering process (Fig. 8) (Ref 63). The vaporization of polymer creates voids between grains, and the sintering of particles diminishes those voids as much as possible. However, some voids remain that may cause shrinkage upon the removal of external energy (Ref 63). In practice, BTO has a measured shrinkage of 26.7% on the *xy* plane and 34.3% along the *z*-direction after sintering at 1330 °C (2425 °F) (Ref 60); similarly, alumina has a total shrinkage of 22.7% after sintering at 1650 °C (3000 °F) (Ref 64), and HA/TCP possesses a shrinkage of 30% after sintering at 1250 °C (2280 °F) (Ref 93) (Fig. 9a–c). Shrinkage not only leads to changes in size of the 3D-printed part but also produces residual stress, which incurs

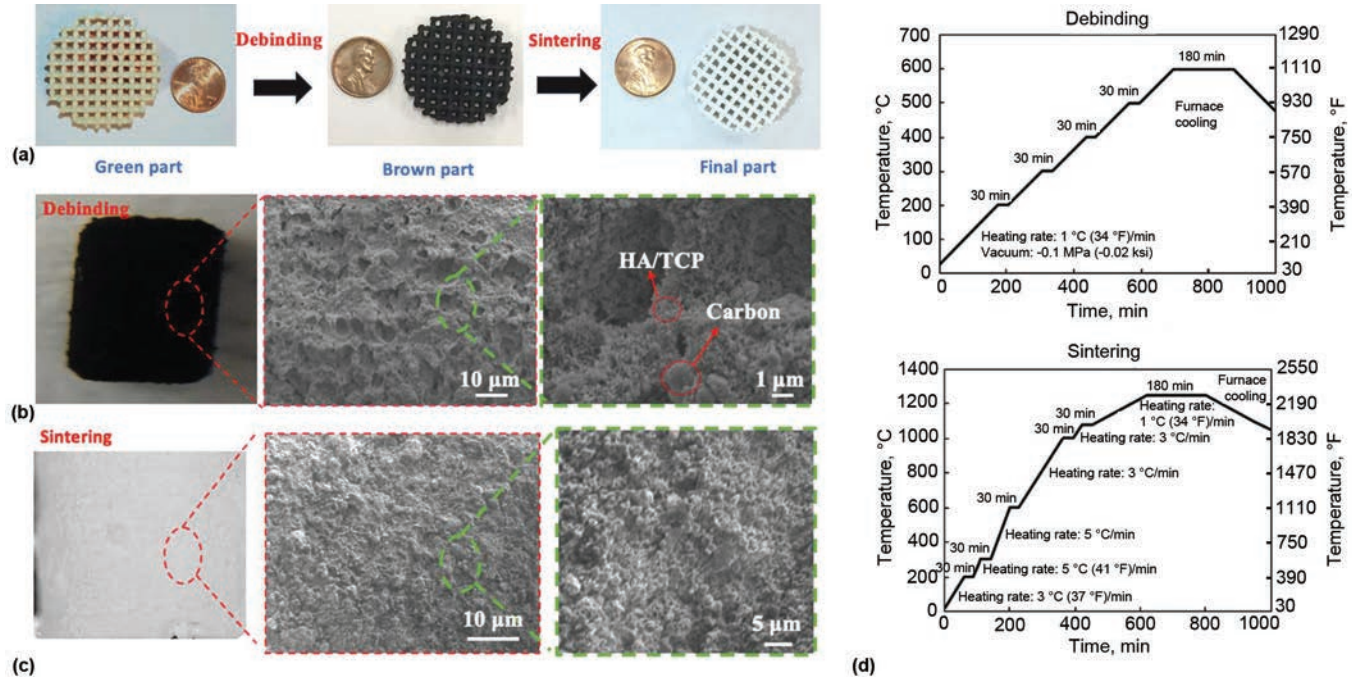

Fig. 8 Postprocessing of a green part printed by the vat-photopolymerization-based ceramic printing process. (a) Ceramic part before and after postprocessing. (b) Scanning electron microscopy (SEM) images of brown part after the debinding process. HA/TCP, hydroxyapatite/tricalcium phosphate. (c) SEM images of final part after the sintering process. (d) Temperature curves of the debinding and sintering processes for fabrication of a bioceramic part

deformation on the part. With the shrinkage problem being the predominant cause of fabrication failures, some compensation methods are considered and investigated to assist in retaining the desired shape during the sintering process.

Various approaches for size compensation in the design phase have been introduced based on modeling of the shrinkage problem. To compensate for uniform shrinkage, the commonly used method is to apply a dimensional offset to the part design at a volume of the statistically computed or actually observed shrinkage scale (Fig. 9d). Therefore, the design must be expanded with the offset operation, to leave stock for a predictable or computable shrinkage that will occur during or after sintering and thus to be close to the truly desired part (Fig. 9e) (Ref 66). In a more complicated but more common case, nonuniform shrinkage is desired; hence, a modern method is mostly based on machine learning techniques, where the dimensional difference between the printed and designed parts is demystified by the mass volume of data training. Accordingly, the dimensional input dumped to the model can derive a predictable result in the shrinkage, and a nonuniform offset can be applicable to the input design (Ref 67–69). Other than the design approaches, there are also some process-related methods to mitigate the shrinkage issue and its consequences. For instance, to compensate the deformation caused by shrinkage and its consequential residual stress, the projection mask image parameters in the MIP-SL process, for example, light intensity, gray scale, and so on, can be altered and fine-tuned to purposely reinforce or weaken suspicious deformation zones (Ref 70, 71).

Property Identification

Porosity

Pores are mostly generated at the debinding process when polymer is pyrolyzed (Ref 58). In the sintering afterward, the highest temperature, usually up to the range from 1200 to 1500 °C (2190 to 2730 °F), would cause densification of the ceramic part (Ref 3, 63). Sintering at such high temperatures is applied to the grain boundaries so that most of the pores disappear during grain growth, while some pores remain and may be difficult to eliminate due to their diffusion paths that are excessively long among the large grains. In most cases, the sintering process diminishes the pores to some extent and also alleviates the negative influences of pores on material properties such as strength (Ref 63). However, there are also certain applications where porosity is desired and important in order to address functional needs, such as cell attachment to scaffolds (Ref 40).

Porosity is determined primarily by sintering temperature, time, and ceramic particle size (Ref 63). Several methods, such as mechanical test, density measurements, porosimetry, gas absorption for surface area, quantitative microscopy, and so on, can be used to gage or evaluate porosity and its variation (Ref 63). In real-world situations, the geometry and arrangement of ceramic particles, although measurable, are usually unpredictable and uncontrollable due to interaction and overlapping among localized mechanisms (Ref 3). Inconsistency and randomness are always associated with porosity, even in the situation where parts are built in the same way using the same material and equipment. Although deviation widely exists, adjusting the sintering temperature and ceramic particle size are proven to be significant factors that can be used to manipulate porosity (Ref 58–60).

Temperature is negatively proportional to the porosity level, meaning that higher sintering temperature usually results in lower porosity, whereas ceramic particle dimension addresses porosity in an opposite way, for example, larger particle size results in larger porosity. Additionally, with all things being equal, the process of sintering has a significant impact on porosity as well. The microwave sintering process outperforms the traditional thermal sintering process in downgrading porosity at the same condition (Ref 40). As a general example of the aforementioned variables, porosity is measured for a part with a desired open porosity of 27% for the sintering of ceramic fabricated by a particle size of 500 μm. At a thermal sintering temperature of 1150 °C (2100 °F), open porosity is approximately 57.87%; at a thermal sintering temperature of 1250 °C (2280 °F), open porosity is reduced to 54.11% (Ref 40). Moving to the case of microwave sintering, open porosity is further reduced to 51.4% at a temperature of 1150 °C (Ref 40). Another designed part has a particle size of 750 nm. In thermal sintering with a temperature of 1150 °C, open porosity is approximately 63.1%; in thermal sintering with a temperature up to 1250 °C, open porosity is also reduced to 58.61%. In comparison, open porosity is approximately 59.76% in microwave sintering at a temperature of 1150 °C (Ref 40).

Lastly, adding dissolvable particles to the material mixture is another effective way of adjusting porosity for the sintering process. An experimental case, where sugar was added to the material, significantly brought the porosity to 50% in the fabrication, based on photocurable resin (Fig. 10) (Ref 72). In addition to sugar, other dissolvable particles such as salt have a similar effect.

Bioceramics Fabrication

With the development of tissue engineering and regenerative medicine, 3D scaffolds with a porous structure have been used for hard tissue regeneration. The porous structure provides enough space for cells to attach and

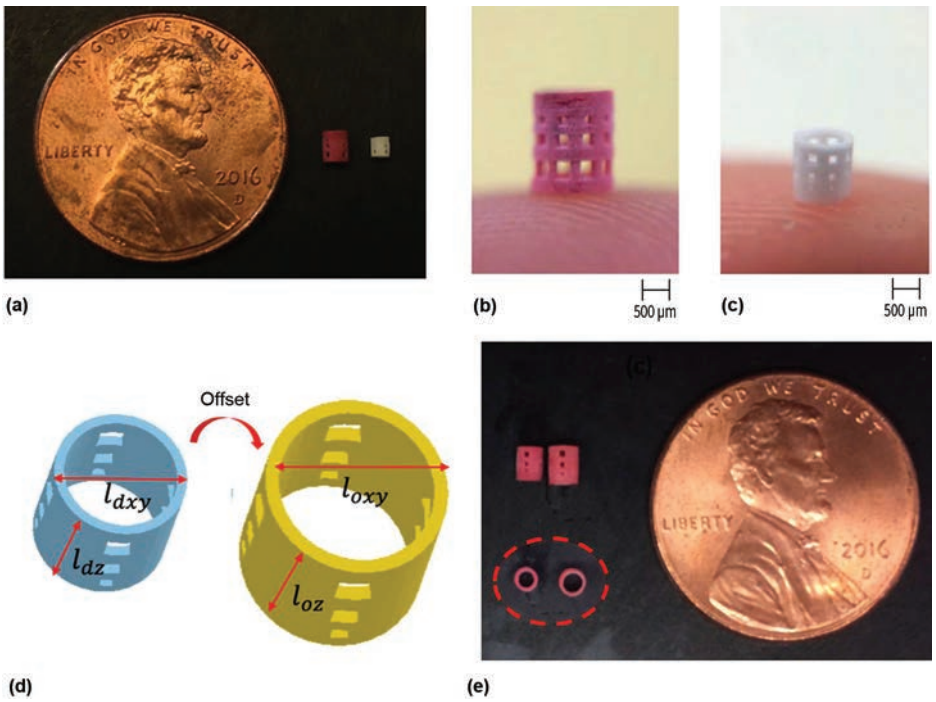

Fig. 9 Shrinkage and compensation in vat photopolymerization (VPP)-based ceramic printing. (a) Ceramic parts before and after postprocessing. (b) Shrinkage of ceramic part fabricated by microscale VPP-based ceramic printing. (c) Final ceramic part after postprocessing. (d) Compensation by redesign of the build-part digital model based on the shrinkage ratio. (e) Green parts before and after compensation. Source: Ref 65

enables blood vessels to deliver nutrition through the inner connective pore network. Bioceramics have been widely used in the fabrication of 3D scaffolds and bone implants due to their good biocompatibility and high mechanical performance (Ref 73). Bioceramics such as hydroxyapatite, calcium phosphate (CAP), bioglass, and graphite show promising properties for tissue engineering applications (Ref 74). Bioceramics fabricated by traditional methods, such as freeze casting (Ref 75), foam replica methods (Ref 76), high-pressure pressing (Ref 77), and particle leaching (Ref 78), can achieve a large range of porosity, but only simple structures can be formed. The VPP-based ceramic printing process can solve these challenges, and biomimetic hierarchical porous structures with high mechanical strength can now be fabricated by using a multiscale VPP process (Ref 79).

For example, a shell-shaped scaffold was designed and fabricated by using MIP-SL for long-bone critical-defect regeneration (Fig. 11a). A photocurable polymer was mixed with 30% (weight/weight) CAP, and the viscosity of this CAP-based slurry was 5375 MPa · s, which is difficult to fabricate using the extrusion-based AM processes. As shown in Fig. 11(a), a 3D scaffold with complex geometric structures was designed based on a digital model of the bone defects. Hierarchical features, ranging from the microscale porous structure (diameter: ~20 to 1000 μm) to interconnected small pores (<5 μm), were accurately fabricated by the VPP-based ceramic printing process (Fig. 11c). The 3D bioceramic scaffold cultured with stem cells was implanted in the long-bone defect, and a large volume of new bone was regenerated with the support of the scaffold after 12 weeks (Fig. 11b). Bioceramics, as one type of biodegradable and biocompatible material, promote the adhesion and proliferation of bone-forming cells (Ref 73, 74), and VPP-based ceramic printing enables fabrication of a complex-shaped bioceramic and facilitates study in the field of hard tissue regeneration (Ref 74, 79).

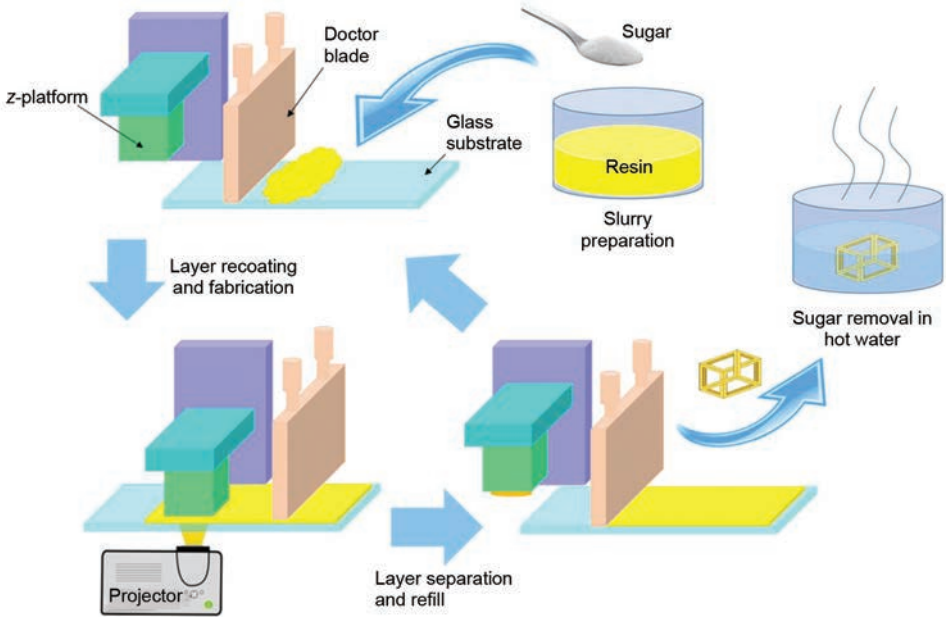

Fig. 10 Porous structure fabrication by the sugar foaming method. Source: Ref 72

Structural Ceramics Fabrication

Structural ceramics are commonly used in industrial applications due to their high-temperature resistance, abrasion resistance, creep resistance, insulativity, and strength (Ref 3, 64). Traditionally, such ceramics are made by a process called dry pressing, which is a pressing method that can only process a relatively large workpiece with simple geometry. With VPP-based ceramic printing, the fabrication of more-complicated geometries is now

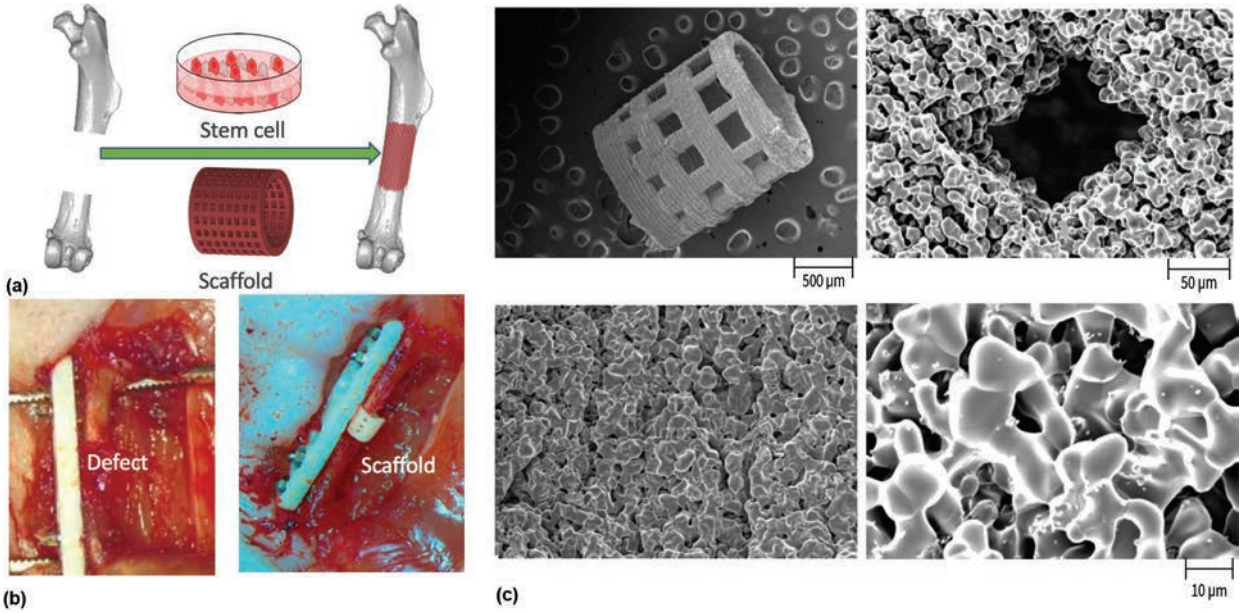

Fig. 11 Calcium phosphate (CAP) scaffold fabricated by the vat-photopolymerization-based printing process for bone regeneration. (a) Three-dimensional scaffold design based on the critical defect of a long bone. (b) The CAP-based scaffold with cultured stem cell was implanted into the long-bone defect. (c) Scanning electron microscopy images of the CAP scaffold under various magnifications.

possible, and smaller-scale ceramic parts can be produced as well. The properties of structural ceramics made by VPP-based ceramic printing are comparable to or even better than dry pressing (Ref 64). Particularly, zirconia-toughened alumina (ZTA) is a popular composite whose mass ratio of alumina to zirconia is 4:1. The ZTA produced by stereolithography-based AM has a density of 4.26 g/cm^3, equivalent to 99.5% relative density, together with a hardness of 17.76 GPa (2.58×10^6 psi), a bending strength of 530.25 MPa (76.89 ksi), and a fracture toughness of 5.72 MPa$\sqrt{m}$ (5.21 ksi$\sqrt{in.}$) (Fig. 12) (Ref 64). Alumina-base ceramics are also one type of structural ceramic that can be fabricated by using the VPP-based process (Ref 80). For example, the green part of an alumina ceramic was printed by using the MIP-SL process. After that, the debinded alumina ceramic part was merged into a liquid precursor infiltration that contained Zr^{4+}, Mg^{2+}, and $Zr^{4+}(Y^{3+})$, and the final ceramic part was obtained by sintering the coated part. By integrating debinding/sintering with liquid precursor infiltration, the grain size of sintered parts was significantly reduced so that the hardness of the alumina ceramic was increased (Ref 80). Recent progress on VPP-based ceramic printing shows the application of ceramic printing as a tool to validate the design and to fabricate the structural ceramic, which reveals a feasible solution to exploring innovations in the field of structural ceramics.

Piezoelectric Ceramics Fabrication

Piezoelectric ceramics are widely known for their superior dielectric properties (Ref 81–84), which are incurred by the short-range distribution of charge within the material. Piezoelectric ceramics have been widely used in inductor applications. When the lattice of the material is subsymmetric, stress can lead to the asymmetric distribution of charge. In this way, tensile and compressive stresses can be interconverted to electric charge. The fabrication of piezoelectric ceramics attracted the interest of many researchers and practitioners due to its remarkable application potential (Ref 81). However, for the same reason of process incapability, the geometry and design of piezoelectric parts is bound by the traditional dry pressing process. The VPP-based ceramic printing, on the other hand, provides a more flexible method when dealing with the geometry of a piezoelectric part.

For example, BTO can be 3D printed using the VPP-based ceramic printing process (Fig. 13). $BaTiO_3$ powders (25 vol%) combined with a mixture of 66 vol% methylethylketone and 34 vol% ethanol were deagglomerated and dried to modify the surface of BTO. The green part was printed by using slurry composed of 70 wt% deagglomerated powders and 30 wt% photocurable resin. After sintering, the density of the final ceramic part achieved 93.7%, and the piezoelectric constant and the relative permittivity were 160 pCN-1 and 1350, respectively (Ref 60). In addition, lead zirconate titanate (PZT) is another type of piezoelectric ceramic that can be fabricated by using VPP-based ceramic printing (Ref 84). The dielectric permittivity of 3D-printed Flex/PZT/Ag composite reaches as high as 120 at 100 Hz with 18 vol% filler, which is approximately 30 times higher than that of pure Flex. Based on this ceramic composite, a capacitor with low resistance was printed, and the capacitance of the 3D-printed capacitor achieved 63 F/g. Because of large material choices and geometry fabrication flexibility, the VPP-based ceramic printing process enables fabrication of piezoelectric ceramics with complex shapes, which further facilitates the research and study of piezo-alike electromagnetic components (Ref 81–84).

Optical Ceramics Fabrication

Optical ceramics play an important role in optical applications due to their high light transmission, wear resistance, and high

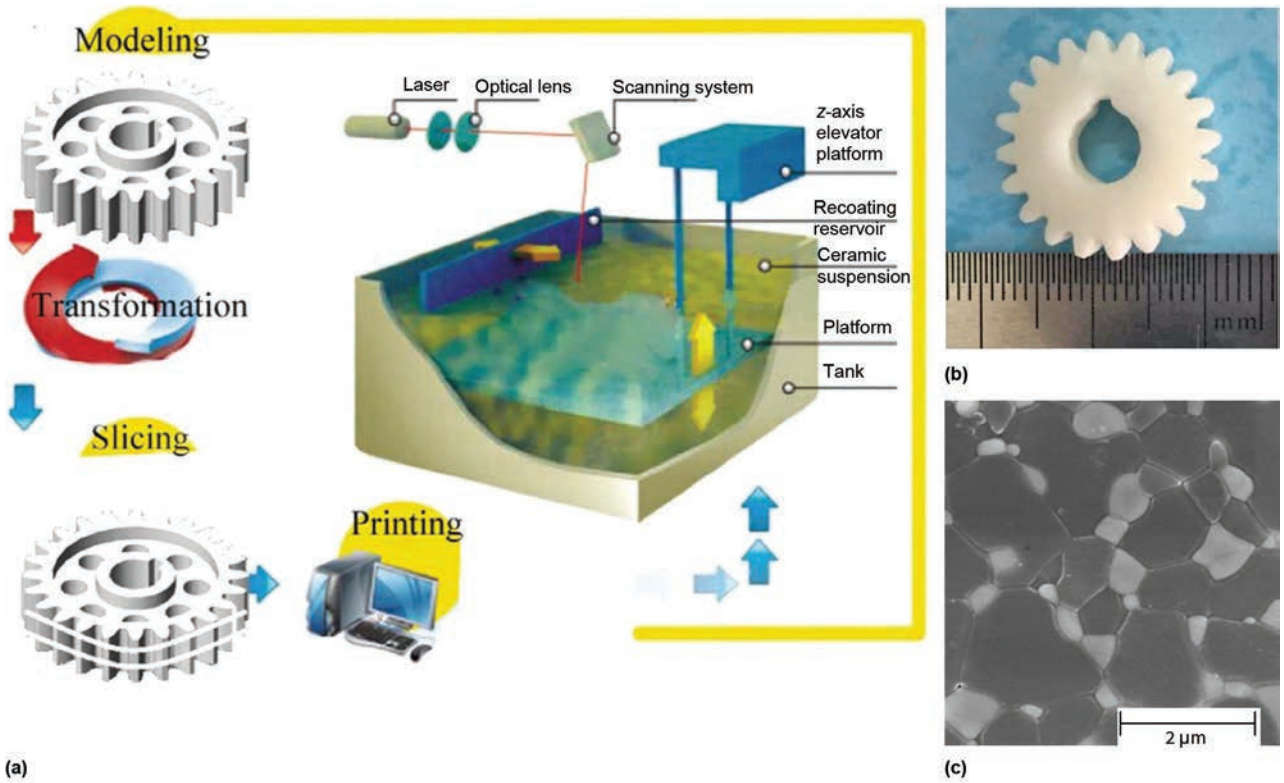

Fig. 12 Zirconia-toughened alumina (ZTA) ceramics fabricated by the vat photopolymerization (VPP)-based printing process, with excellent mechanical properties. (a) Schematic illustration of the VPP-based ceramic printing process. (b) Gear-shaped ZTA ceramic printed through the VPP-based printing process. (c) Microstructure of polished ZTA ceramic after sintering at 1600 °C (2910 °F). Source: Ref 64

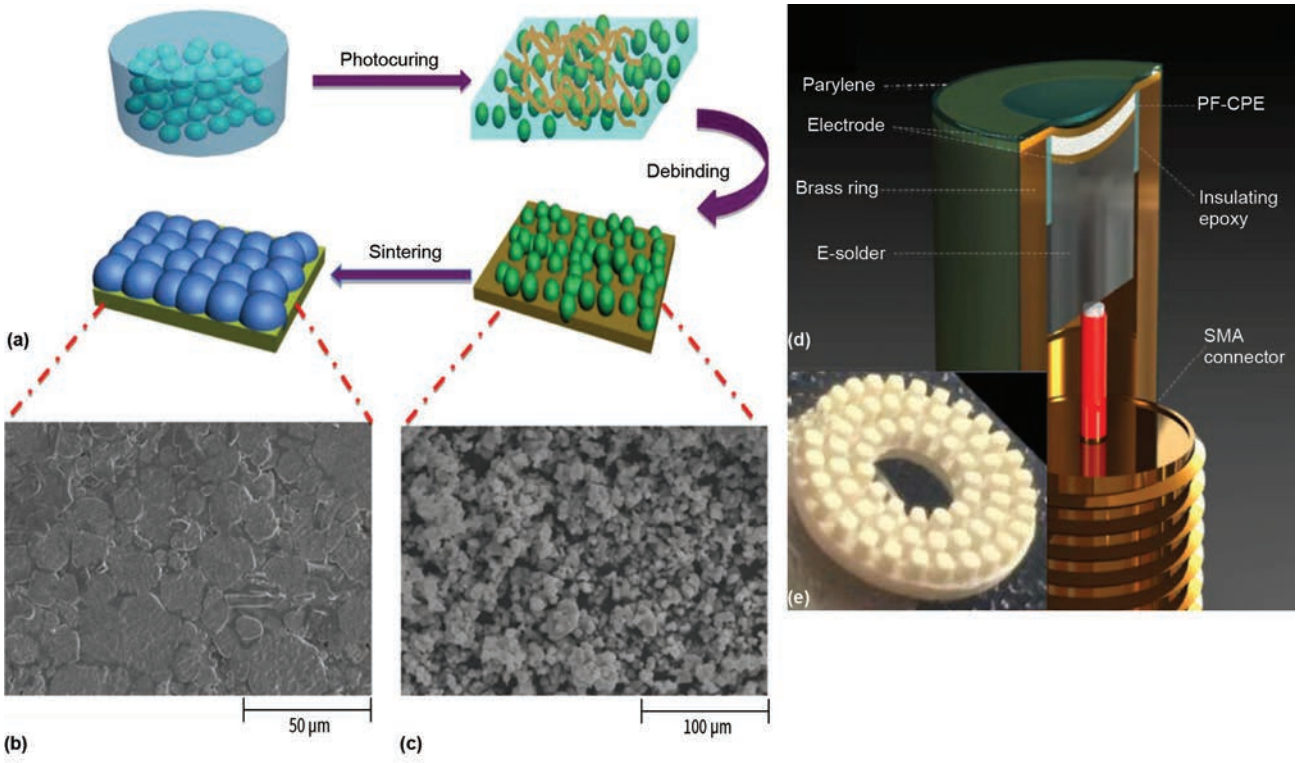

Fig. 13 Piezoelectric ceramic fabricated by the vat photopolymerization (VPP)-based printing process for energy focusing and ultrasonic sensing. (a) Diagram of green-part fabrication using VPP-based printing. (b) Scanning electron microscopy (SEM) image of sintered sample after 6 h sintering at 1330 °C (2425 °F). (c) SEM image of sample after the debinding process. (d) Profile of a transducer. PF-CPE, printing-focused concave-shaped piezoelectric element; SMA, subminiature version A. (e) Image of three-dimensional-segment annular array with 64 pillars that were irregularly distributed. Source: Ref 60

strength, which are hard to achieve with optical plastics (Ref 41, 85). However, it is difficult to form optical ceramics, such as glass, crystals, alumina, and so on, into complex 3D shapes with fine features by using the traditional molding process (Ref 20). Additive manufacturing opens a new door for the next generation of optical devices by taking advantage of optical ceramics (Ref 20). Much effort has been made in the field of optical ceramic printing (Ref 41, 85, 86). For example, transparent glass can be directly printed by the filament-fed laser-heated process, in which glass is heated to more than 1000 °C (1830 °F) (Ref 85). However, the printed structures cannot be used in industrial applications due to insufficient heating and imperfect surface quality (Ref 86).

Benefiting from the advantages of VPP-based ceramic printing, both the surface quality and the complex geometry of 3D-printed glass were improved. For example, 37.5% (volume/volume) silicon particles were mixed with a photocurable polymer, and the green part was built with the nanocomposite by the VPP-based ceramic printing process (Fig. 14a) (Ref 41). After debinding and sintering, the inner polymer was removed, and the bulk density of the 3D-printed part increased dramatically. The shrinkage ratio of the 3D-printed optical glass was 27.88%, and both microscale and macroscale optical structures were successfully fabricated by using this approach (Fig. 14b) (Ref 41). More specifically, in the axial direction, the stair effect is obvious in the area between two adjacent bonding layers, because the photocurable composite is accumulated using the layer-based manner (Fig. 14c) (Ref 41); in the radial direction, the roughness of the printed part is acceptable, which is smaller than 2 nm (Ref 41). As shown in Fig. 14(c), the optical transparency of the 3D-printed glass is comparable with commercial fused silica (Ref 41). In general, VPP-based ceramic printing provides a mold-free formation method of constructing 3D optical structures and can widen optical applications of optical ceramics in the future.

Polymer-Derived Ceramics Fabrication

Polymer-derived ceramics have been widely developed and used in fields such as biomedical components, electromechanical systems (micro- and nanolevels), environmental studies, transportation, information technology, and so on (Ref 87–92). Polymer-derived ceramics have many promising functional properties, including high strength, thermal and creep resistance, and stability in chemistry environments (oxidation and corrosion) (Ref 87). More and more, electrical energy storage uses polymer-derived ceramics, and polymer-derived ceramic anodes provide a significant improvement in reversible capacity values and stability in electrochemical cycling compared to the graphite-based anodes that are commonly used now (2020) (Ref 91).

In polymer-derived ceramics fabrication, instead of a slurry composed of photocurable resin and ceramic particles, 3D-shaped ceramics can be obtained by using only photocurable polymers with special elemental chemical bonds. The material used in the polymer-derived ceramics process is usually based on the Si-O-C-N-B chemical bond system (Ref 87). In polymer-derived ceramics fabrication, the green part is printed by the VPP-based printing process, including stereolithography and TPP. The green part is then sintered at 900 to 1000 °C (1650 to 1830 °F) to obtain the final ceramic, including silicon carbide (SiC), silicon nitride (Si_3N_4), boron nitride (BN), aluminum nitride (AlN), silicon oxycarbide (SiOC), silicon carbonitride (SiCN), boron carbonitride (BCN), and so on (Ref 87–92).

For example, SiOC microlattices with various designs were fabricated by using the polymer-derived ceramics fabrication method (Fig. 15a–d). The green part was pyrolyzed for 1 h at 1000 °C (1830 °F) in a nitrogen environment, and the compression strength of the final SiOC was 0.686 MPa (0.099 ksi) (Ref 87). Not only can microscale and macroscale

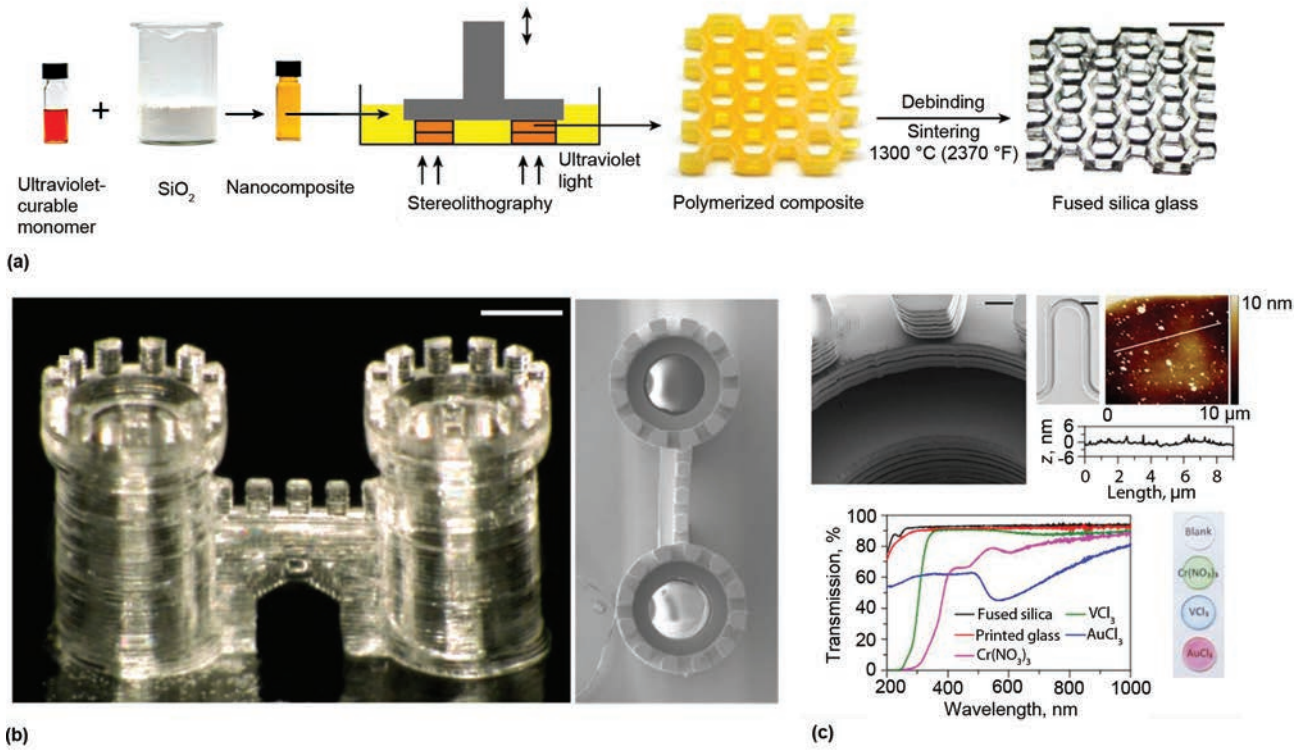

Fig. 14 Glass fabricated by the vat photopolymerization (VPP)-based printing process for optical purposes. (a) Silica-nanopowder-based material printed by the VPP-based printing process. (b) Three-dimensional (3D)-printed fused silica glass with microstructures. (c) Surface quality and optical performance of 3D-printed glass. Source: Ref 41

ceramics be fabricated by this approach (Fig. 15e), but nanoscale ceramics can also be fabricated using the VPP-based ceramic printing process, and the fabricated nanoscale ceramics show extraordinary mechanical performance (Ref 92). For example, a glassy carbon nanolattice was manufactured by the TPP process (Ref 92). The printed part was then pyrolyzed at 900 °C (1650 °F) in a vacuum circumstance, and the final part exhibited 20% shrinkage (Fig. 15f). This 3D-printed carbon nanolattice structure exhibited a compression strength of 1.2 GPa (0.17×10^6 psi) at a density of 0.6 g/cm^3. The VPP-based polymer-derived ceramics printing process provides more opportunities to construct temperature-resistant, ultralight, and ultrastiff ceramic structures with features ranging from macroscale to nanoscale, and 3D-printed polymer-derived ceramics possess the prospect of being used in many applications that require ceramic structures.

Summary and Outlook

In general, VPP is an enhanced AM method for ceramic fabrication with major advantages in its multiscale capability and printing speed (Ref 3, 45–48). Scalewise, VPP is versatile for fabrication ranging from as large as a few meters to as small as several micrometers (Ref 23, 25–33). Throughout the span of its dimensional capabilities, VPP also maintains relatively fast printing speed, whereas other methods, such as SLS or binder jetting, may sacrifice building speed for large cross-sectional parts due to traversing of the tool bit and time-consuming material spreading over a large area (Ref 30, 31). Additionally, VPP is not compromised by the special complexity that it can achieve, and it is even advantageous in the fabrication of overhanging structures, where the slurry-based material provides sufficient self-support as a result of its viscosity and density (Ref 53, 54). Moreover, the cross section of a part printed by AM processes such as FDM and SLM shows anisotropic grain structures, which generate orientation dependence in physical properties. A printed part using the VPP-based ceramic manufacturing approach shows superior grain isotropy compared with most of the ceramic AM processes (Ref 80). This isotropic ceramic distribution improves the mechanical performance of the 3D-printed part. Overall, the revolution of the VPP-based ceramic manufacturing process has brought new opportunities in producing ceramic products with complex geometric shapes (Ref 2, 5, 93). Many different types of ceramic materials, which are difficult to fabricate using the traditional manufacturing processes, can be built into 3D shapes using the VPP-based ceramic manufacturing process (Ref 20, 21, 46, 93). The manufacturing capability of the VPP-based ceramic manufacturing process enables engineers to expand ceramics applications in future engineering systems.

While VPP offers many advantages in ceramic fabrication, there are also several issues to address (Ref 3, 45–48). First, to maintain the curing capability of the slurry mixture material, the density of ceramic is capped to a point that can guarantee cross linking when mixed with photocurable polymers (Ref 3). For the same reason, both the slurry curing time during fabrication and the ceramic binding force during consolidation are subject to the limitation of the ratio of ceramic particles to photocurable polymer (Ref 3). Insufficient photocurable polymer in the mixture is the reason for elongated curing time during fabrication; inversely, a lack of ceramic ingredient causes inferior binding force and may result in poor yield in the sintering process. Meanwhile, when dealing with large-dimension parts, the sintering process is subject to excessive process variation due to the inconsistency of the slurry material (Ref 64, 77). Nonhomogeneous slurry with nonuniform distribution of ceramic particles causes different shrinkage during the sintering process, and large parts easily trap air and gas during the sintering process, preventing a timely escape of air from the solid part and thus forming cracks (Ref 3). The reproducibility of sintering a part is therefore

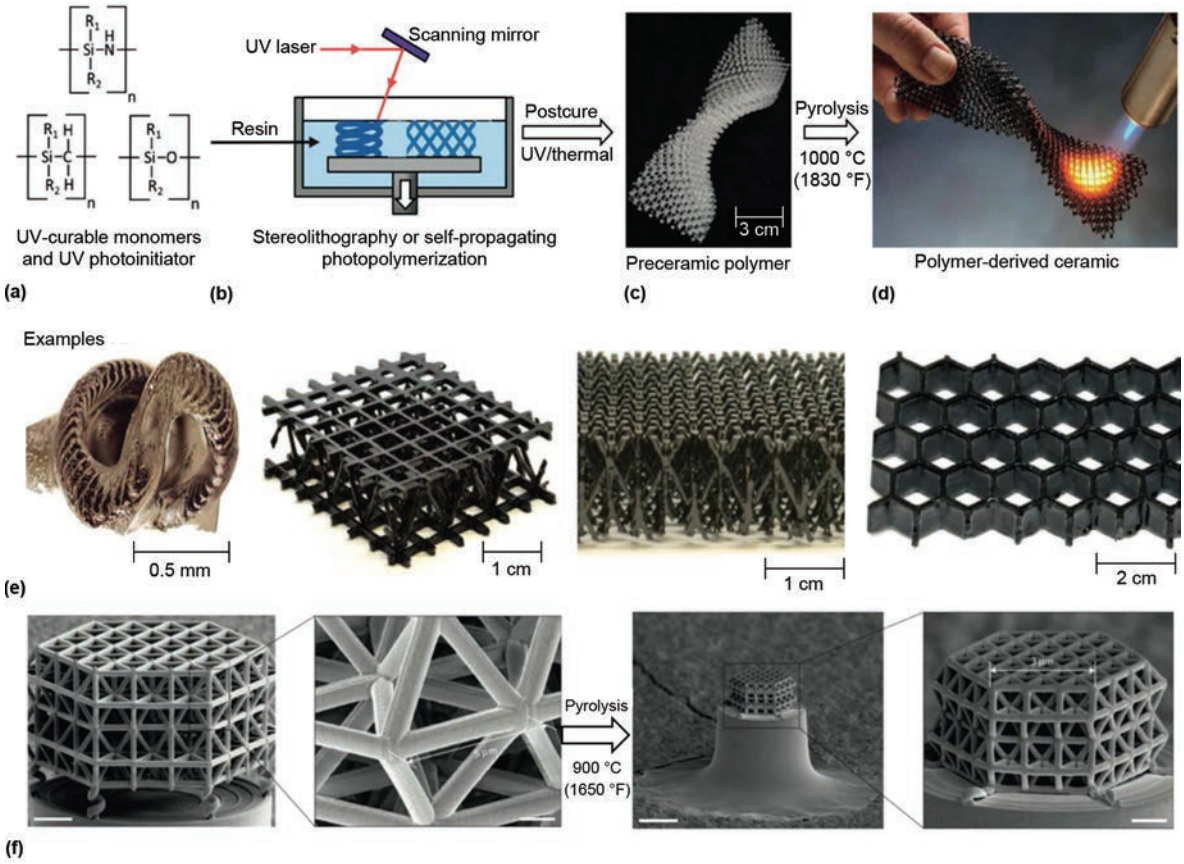

Fig. 15 Vat photopolymerization (VPP)-based ceramic fabrication using polymer-derived ceramics. (a) Photocurable material used in the polymer-derived ceramics process. UV, ultraviolet. Source: Ref 87. (b) Printing process for polymer-derived ceramics. Source: Ref 87. (c) Printed green part. Source: Ref 87. (d) Final ceramic part after pyrolysis. Source: Ref 87. (e) Polymer-derived ceramics with various shapes printed by the VPP-based process. Source: Ref 87. (f) Three-dimensional-printed ceramic object with nanolattice. Source: Ref 92

hard to maintain at large volume, consequently restricting the VPP process to being reasonable and suitable for a complex part at a large dimensional size (Ref 63). Finally, the slurry mixture is also vital to the blade-based spread process, because viscosity is directly related to the spreading quality of thin layers (Ref 3, 48).

However, all of these challenges are presumably solvable, because many technology advances have recently been made. For instance, the overwhelming problem of process inconsistency and variance can potentially be modeled, analyzed, and addressed by artificial-intelligence-based computation, in the way that the computer-aided design model for printing and sintering can be compensated on a prefabrication basis to cover predictable variances on the go (Ref 67–71). For the AM process itself, recent investigation reveals that the surface quality of parts can be further enhanced in several feasible ways by removing the stair effect caused by the layer-based processes (Ref 30, 31, 44). Also, the material scope will not be restricted to one single type of ceramic, because research is in the process of achieving multimaterial fabrication within a single part and under a single fabrication run (Ref 28, 38).

REFERENCES

1. B. Murat, *Engineering Ceramics*, Springer Science and Business Media, 2013, p 406–444
2. Z. Chen, Z. Li, J. Li, C. Liu, C. Lao, Y. Fu, C. Liu, Y. Li, P. Wang, and Y. He, 3D Printing of Ceramics: A Review, *J. Eur. Ceram. Soc.*, Vol 39, April 2019, p 661–687
3. V. Tomeckova and J.W. Halloran, Predictive Models for the Photopolymerization of Ceramic Suspensions, *J. Eur. Ceram. Soc.*, Vol 30 (No. 14), 2010, p 2833–2840
4. J. Edgar and S. Tint, Additive Manufacturing Technologies: 3D Printing, Rapid Prototyping, and Direct Digital Manufacturing, *Johnson Matthey Tech.*, Vol 59 (No. 3), 2015, p 193–198
5. K.V. Wong and A. Hernandez, A Review of Additive Manufacturing, *Int. Scholar. Res. Notices, Mech. Eng.*, Vol 2012, 2012
6. T.D. Ngo, A. Kashani, G. Imbalzano, K.T. Nguyen, and D. Hui, Additive Manufacturing (3D Printing): A Review of Materials, Methods, Applications and Challenges, *Compos. B: Eng.*, Vol 143, June 2018, p 172–196
7. B. Derby, Inkjet Printing Ceramics: From Drops to Solid, *J. Eur. Ceram. Soc.*, Vol 31 (No. 14), 2011, p 2543–2550
8. J.A. Gonzalez, J. Mireles, Y. Lin, and R.B. Wicker, Characterization of Ceramic Components Fabricated Using Binder Jetting Additive Manufacturing Technology, *Ceram. Int.*, Vol 42 (No. 9), 2016, p 10559–10564
9. J.P. Kruth, P. Mercelis, J. Van Vaerenbergh, L. Froyen, and M. Rombouts, Binding Mechanisms in Selective Laser Sintering and Selective Laser Melting, *Rapid Prototyp. J.*, Vol 11 (No. 1), 2005, p 26–36
10. P.F.D.M. Dudek, FDM 3D Printing Technology in Manufacturing Composite Elements, *Arch. Metall. Mater.*, Vol 58 (No. 4), 2013, p 1415–1418
11. G. Rundle, *A Revolution in the Making*, Simon and Schuster, June 2014

12. M. Allahverdi, S.C. Danforth, M. Jafari, and A. Safari, Processing of Advanced Electroceramic Components by Fused Deposition Technique, *J. Eur. Ceram. Soc*., Vol 21 (No. 10–11), 2001, p 1485–1490
13. H. Yang, S. Yang, X. Chi, and J.R. Evans, Fine Ceramic Lattices Prepared by Extrusion Freeforming, *J. Biomed. Mater. Res. B*, Vol 79 (No. 1), 2006, p 116–121
14. D.W. Hutmacher, T. Schantz, I. Zein, K.W. Ng, S.H. Teoh, and K.C. Tan, Mechanical Properties and Cell Cultural Response of Polycaprolactone Scaffolds Designed and Fabricated via Fused Deposition Modeling, *Biomed. Mater. Res*., Vol 55 (No. 2), 2001, p 203–216
15. T. Cao, K.H. Ho, and S.H. Teoh, Scaffold Design and In Vitro Study of Osteochondral Coculture in a Three-Dimensional Porous Polycaprolactone Scaffold Fabricated by Fused Deposition Modeling, *Tissue Eng*., Vol 9 (No. 4, Supplement 1), 2003, p 103–112
16. M.W. Sa, B.N.B. Nguyen, R.A. Moriarty, T. Kamalitdinov, J.P. Fisher, and J.Y. Kim, Fabrication and Evaluation of 3D Printed BCP Scaffolds Reinforced with ZrO_2 for Bone Tissue Applications, *Biotechnol. Bioeng*., Vol 115 (No. 4), 2018, p 989–999
17. J.A. Lewis and G.M. Gratson, Direct Writing in Three Dimensions, *Mater. Today*, Vol 7 (No. 7–8), 2004, p 32–39
18. E. Feilden, E.G.T. Blanca, F. Giuliani, E. Saiz, and L. Vandeperre, Robocasting of Structural Ceramic Parts with Hydrogel Inks, *J. Eur. Ceram. Soc*., Vol 36 (No. 10), 2016, p 2525–2533
19. S. Michna, W. Wu, and J.A. Lewis, Concentrated Hydroxyapatite Inks for Direct-Write Assembly of 3D Periodic Scaffolds, *Biomaterials*, Vol 26 (No. 28), 2005, p 5632–5639
20. Y. Yang, X. Song, X. Li, Z. Chen, C. Zhou, Q. Zhou, and Y. Chen, Recent Progress in Biomimetic Additive Manufacturing Technology: From Materials to Functional Structures, *Adv.Mater*., Vol 30 (No. 36), 2018, p 1706539
21. Y.S. Leung, T.H. Kwok, X. Li, Y. Yang, C.C. Wang, and Y. Chen, Challenges and Status on Design and Computation for Emerging Additive Manufacturing Technologies, *J. Comput. Inf. Sci. Eng*., Vol 19 (No. 2), 2019, p 021013
22. B. Mueller, Additive Manufacturing Technologies—Rapid Prototyping to Direct Digital Manufacturing, *Assem. Autom*., Vol 32 (No. 2), 2012
23. P.F. Jacobs, *Stereolithography and Other RPM Technologies: From Rapid Prototyping to Rapid Tooling*, Society of Manufacturing Engineers, 1995, p 59–79
24. Y. Yang, X. Li, X. Zheng, Z. Chen, Q. Zhou, and Y. Chen, 3D-Printed Biomimetic Super- Hydrophobic Structure for Microdroplet Manipulation and Oil/Water Separation, *Adv. Mater*., Vol 30 (No. 9), 2018, p 1704912
25. X. Li and Y. Chen, Micro-Scale Feature Fabrication Using Immersed Surface Accumulation, *J. Manuf. Process*., Vol 28, 2017, p 531–540
26. H. Mao, Y.S. Leung, Y. Li, P. Hu, W. Wu, and Y. Chen, Multiscale Stereolithography Using Shaped Beams, *J. Micro Nano-Manuf*., Vol 5 (No. 4), 2017, p 040905
27. Y. Pan, C. Zhou, and Y. Chen, A Fast Mask Projection Stereolithography Process for Fabricating Digital Models in Minutes, *ASME J. Manuf. Sci. Eng*., Vol 134 (No. 5), 2012, p 051011
28. C. Zhou, Y. Chen, Z. Yang, and B. Khoshnevis, Digital Material Fabrication Using Mask-Image-Projection-Based Stereolithography, *Rapid Prototyp. J*., Vol 19 (No. 3), 2013, p 153–165
29. C. Zhou and Y. Chen, Additive Manufacturing Based on Optimized Mask Video Projection for Improved Accuracy and Resolution, *J. Manuf. Process*., Vol 14 (No. 2), 2012, p 107–118
30. X. Li, H. Mao, Y. Pan, and Y. Chen, Mask Video Projection-Based Stereolithography with Continuous Resin Flow, *ASME J. Manuf. Sci. Eng*., Vol 141 (No. 8), 2019, p 081007, doi:10.1115/1.4043765
31. J.R. Tumbleston, D. Shirvanyants, N. Ermoshkin, R. Januszieicz, A.R. Johnson, D. Kelly, K. Chen, R. Pinschmidt, J.P. Rolland, A. Ermoshkin, and E.T. Samulski, Continuous Liquid Interface Production of 3D Objects, *Science*, Vol 347 (No. 6228), 2015, p 1349–1352
32. Y. Yang, X. Li, M. Chu, H. Sun, J. Jin, K. Yu, Q. Wang, Q. Zhou, and Y. Chen, Electrically Assisted 3D Printing of Nacre-Inspired Structures with Self-Sensing Capability, *Sci. Adv*., Vol 5 (No. 4), 2019, p 9490
33. X. Li, B. Xie, J. Jin, Y. Chai, and Y. Chen, 3D Printing Temporary Crown and Bridge by Temperature Controlled Mask Image Projection Stereolithography, *Proced. Manuf*., Vol 26, 2018, p 1023–1033
34. A. Ovsianikov, B. Chichkov, P. Mente, N.A. Monteiro-Riviere, A. Doraiswamy, and R.J. Narayan, Two Photon Polymerization of Polymer-Ceramic Hybrid Materials for Transdermal Drug Delivery, *Int. J. Appl. Ceram.Technol*., Vol 4 (No. 1), 2007, p 22–29
35. X. Li, T. Baldacchin, X. Song, and Y. Chen, Multi-Scale Additive Manufacturing: An Investigation on Building Objects with Macro-, Micro- and Nano-Scales Features, *11th International Conference on Micro Manufacturing*, March 2016 (Irvine, CA), p 29–31
36. J. Zhang, Y. Yang, B. Zhu, X. Li, J. Jin, Z. Chen, Y. Chen, and Q. Zhou, Multifocal Point Beam Forming by a Single Ultrasonic Transducer with 3D Printed Holograms, *Appl. Phys. Lett*., Vol 113 (No. 24), 2018, p 243502
37. P.J. Bartolo and J. Gaspar, Metal Filled Resin for Stereolithography Metal Part, *CIRP Ann*., Vol 57 (No. 1), 2008, p 235–238
38. X. Li, Y. Yang, B. Xie, M. Chu, H. Sun, S. Hao, Y. Chen, and Y. Chen, 3D Printing of Flexible Liquid Sensor Based on Swelling Behavior of Hydrogel with Carbon Nanotubes, *Adv. Mater. Technol*., Vol 4 (No. 2), 2019, p 1800476
39. X. Zheng, H. Lee, T.H. Weisgraber, M. Shusteff, J. DeOtte, E.B. Duoss, J.D. Kuntz, M.M. Biener, Q. Ge, J.A. Jackson, and S.O. Kucheyev, Ultralight, Ultrastiff Mechanical Metamaterials, *Science*, Vol 344 (No. 6190), 2014, p 1373–1377
40. S. Tarafder, V.K. Balla, N.M. Davies, A. Bandyopadhyay, and S. Bose, Microwave-Sintered 3D Printed Tricalcium Phosphate Scaffolds for Bone Tissue Engineering, *J. Tissue Eng. Regen. M*, Vol 7 (No. 8), 2013, p 631–641
41. F. Kotz, K. Arnold, W. Bauer, D. Schild, N. Keller, K. Sachsenheimer, T.M. Nargang, C. Richter, D. Helmer, and B.E. Rapp, Three-Dimensional Printing of Transparent Fused Silica Glass, *Nature*, Vol 544 (No. 7650), 2017, p 337
42. Y. Pan, X. Zhao, C. Zhou, and Y. Chen, Smooth Surface Fabrication in Mask Projection Based Stereolithography, *J. Manuf. Process*., Vol 14 (No. 4), 2012, p 460–470
43. M. Vaezi, H. Seitz, and S. Yang, A Review on 3D Micro-Additive Manufacturing Technologies, *Int. J. Adv. Manuf. Technol*., Vol 67 (No. 5–8), 2013, p 1721–1754
44. F.P. Melchels, J. Feijen, and D.W. Grijpma, A Review on Stereolithography and Its Applications in Biomedical Engineering, *Biomaterials*, Vol 31 (No. 24), 2010, p 6121–6130
45. K.C. Wu, "Parametric Study and Optimization of Ceramic Stereolithography," University of Michigan, 2005
46. G.A. Brady and J.W. Halloran, Stereolithography of Ceramic Suspensions, *Rapid Prototyp. J*., Vol 3 (No. 2), 1997, p 61–65
47. X. Zhang, X.N. Jiang, and C. Sun, Micro-Stereolithography of Polymeric and Ceramic Microstructures, *Sens. Actuators A: Physical*, Vol 77 (No. 2), 1999, p 149–156
48. X. Song, Y. Chen, T.W. Lee, S. Wu, and L. Cheng, Ceramic Fabrication Using Mask-Image-Projection-Based Stereolithography Integrated with Tape-Casting, *J. Manuf. Process*., Vol 20, 2015, p 456–464
49. I. Gibson, D. Rosen, and B. Stucker, Vat Photopolymerization Processes, *Addit. Manuf. Technol*., 2015, p 63–106
50. Y.T. Chou, Y.T. Ko, and M.F. Yan, Fluid Flow Model for Ceramic Tape Casting, *J. Am. Ceram. Soc*., Vol 70 (No. 10), 1987, p C-280
51. J. Huang, T.H. Kwok, C. Zhou, and W. Xu, Surfel Convolutional Neural Network

for Support Detection in Additive Manufacturing, *Int. J. Adv. Manuf. Technol*., Vol 102, 2019, p 1–12
52. J. Jin and Y. Chen, Highly Removable Water Support for Stereolithography, *J. Manuf. Process*., Vol 28, 2017, p 541–549
53. L. He and X. Song, Supportability of a High-Yield-Stress Slurry in a New Stereolithography-Based Ceramic Fabrication Process, *JOM*, Vol 70 (No. 3), 2018, p 407–412
54. L. He, F. Fei, W. Wang, and X. Song, Support-Free Ceramic Stereolithography of Complex Overhanging Structures Based on an Elasto-Viscoplastic Suspension Feedstock, *ACS Appl. Mater. Interfaces*, Vol 11, 2019, p 18849–18857
55. L. Xu, Q. Huang, A. Sabbaghi, and T. Dasgupta, Shape Deviation Modeling for Dimensional Quality Control in Additive Manufacturing, *ASME 2013 International Mechanical Engineering Congress and Exposition,* Vol 2A, American Society of Mechanical Engineers, Nov 2013, p V02AT02A018
56. J.G. Zhou, D. Herscovici, and C.C. Chen, Parametric Process Optimization to Improve the Accuracy of Rapid Prototyped Stereolithography Parts, *Int. J. Mach. Tools Manuf*., Vol 40 (No. 3), 2000, p 363–379
57. K. Xu and Y. Chen, Photocuring Temperature Study for Curl Distortion Control in Projection- Based Stereolithography, *J. Manuf. Sci. Eng*., Vol 139 (No. 2), 2017, p 021002
58. H. Wu, Y. Cheng, W. Liu, R. He, M. Zhou, S. Wu, X. Song, and Y. Chen, Effect of the Particle Size and the Debinding Process on the Density of Alumina Ceramics Fabricated by 3D Printing Based on Stereolithography, *Ceram. Int*., Vol 42 (No. 15), 2016, p 17290–17294
59. M. Zhou, W. Liu, H. Wu, X. Song, Y. Chen, L. Cheng, F. He, S. Chen, and S. Wu, Preparation of a Defect-Free Alumina Cutting Tool via Additive Manufacturing Based on Stereolithography—Optimization of the Drying and Debinding Processes, *Ceram. Int*., Vol 42 (No. 10), 2016, p 11598–11602
60. Z. Chen, X. Song, L. Lei, X. Chen, C. Fei, C.T. Chiu, X. Qian, T. Ma, Y. Yang, K. Shung, and Y. Chen, 3D Printing of Piezoelectric Element for Energy Focusing and Ultrasonic Sensing, *Nano Energy*, Vol 27, 2016, p 78–86
61. R.V. Oliveira, V. Soldi, M.C. Fredel, and A.T. Pires, Ceramic Injection Moulding: Influence of Specimen Dimensions and Temperature on Solvent Debinding Kinetics, *J. Mater. Process. Technol*., Vol 160 (No. 2), 2005, p 213–220
62. Z. Xie, Y. Huang, J. Wu, and L. Zheng, Microwave Debinding of a Ceramic Injection Moulded Body, *J. Mater. Sci. Lett*., Vol 14 (No. 11), 1995, p 794–795
63. M.N. Rahaman, *Ceramic Processing and Sintering*, CRC Press, 2003
64. W. Liu, H. Wu, M. Zhou, R. He, Q. Jiang, Z. Wu, Y. Cheng, X. Song, Y. Chen, and S. Wu, Fabrication of Fine-Grained Alumina Ceramics by a Novel Process Integrating Stereolithography and Liquid Precursor Infiltration Processing, *Ceram. Int*., Vol 42 (No. 15), 2016, p 17736–17741
65. X. Li, Y. Yuan, et al., 3D Printing of Hydroxyapatite/Tricalcium Phosphate Scaffold with Hierarchical Porous Structure for Bone Regeneration, *Bio-Design and Manufacturing*, Vol 3 (No. 1), 2020, p 15–29
66. Y. Chen and C.C. Wang, Uniform Offsetting of Polygonal Model Based on Layered Depth-Normal Images, *Comput.-Aided Des*., Vol 43 (No. 1), 2011, p 31–46
67. Z. Zhu, N. Anwer, Q. Huang, and L. Mathieu, Machine Learning in Tolerancing for Additive Manufacturing, *CIRP Ann*., Vol 67 (No. 1), 2018, p 157–160
68. Q. Huang, 3D Printing Shrinkage Compensation Using Radial and Angular Layer Perimeter Point Information, U.S. Patent 9,886,526, 2018
69. Q. Huang, H. Nouri, K. Xu, Y. Chen, S. Sosina, and T. Dasgupta, Statistical Predictive Modeling and Compensation of Geometric Deviations of Three-Dimensional Printed Products, *J. Manuf. Sci. Eng*., Vol 136 (No. 6), 2014, p 061008
70. K. Xu and Y. Chen, Mask Image Planning for Deformation Control in Projection-Based Stereolithography Process, *J. Manuf. Sci. Eng*., Vol 137 (No. 3), 2015, p 031014
71. K. Xu, T.H. Kwok, Z. Zhao, and Y. Chen, A Reverse Compensation Framework for Shape Deformation Control in Additive Manufacturing, *J. Comput. Inf. Sci. Eng*., Vol 17 (No. 2), 2017, p 021012
72. X. Song, Z. Zhang, Z. Chen, and Y. Chen, Porous Structure Fabrication Using a Stereolithography-Based Sugar Foaming Method, *J. Manuf. Sci. Eng*., Vol 139 (No. 3), 2017, p 031015
73. T. Thamaraiselvi and S. Rajeswari, Biological Evaluation of Bioceramic Materials—A Review, *Carbon*, Vol 24 (No. 31), 2004, p 172
74. A. El-Ghannam, Bone Reconstruction: From Bioceramics to Tissue Engineering, *Expert Rev. Medical Dev*., Vol 2 (No. 1), 2005, p 87–101
75. A. Macchetta, I.G. Turner, and C.R. Bowen, Fabrication of HA/TCP Scaffolds with a Graded and Porous Structure Using a Camphene-Based Freeze-Casting Method, *Acta Biomater*., Vol 5 (No. 4), 2009, p 1319–1327
76. X. Miao, D.M. Tan, J. Li, Y. Xiao, and R. Crawford, Mechanical and Biological Properties of Hydroxyapatite/Tricalcium Phosphate Scaffolds Coated with Poly (Lactic-Co-Glycolic Acid), *Acta Biomater*., Vol 4 (No. 3), 2008, p 638–645
77. A. Nakahira, T. Murakami, T. Onoki, T. Hashida, and K. Hosoi, Fabrication of Porous Hydroxyapatite Using Hydrothermal Hot Pressing and Post-Sintering, *J. Am. Ceram. Soc*., Vol 88 (No. 5), 2005, p 1334–1336
78. A. Rakovsky, I. Gotman, E. Rabkin, and E.Y. Gutmanas, β-TCP-Polylactide Composite Scaffolds with High Strength and Enhanced Permeability Prepared by a Modified Salt Leaching Method, *J. Mech. Behav. Biomed*., Vol 32, 2014, p 89–98
79. R. Alluri, X. Song, S. Bougioukli, W. Pannell, V. Vakhshori, O. Sugiyama, A. Tang, S.H. Park, Y. Chen, and J.R. Lieberman, Regional Gene Therapy with 3D Printed Scaffolds to Heal Critical Sized Bone Defects in a Rat Model, *J. Biomed. Mater. Res. A*, 2019, p 1–9
80. H. Wu, W. Liu, R. He, Z. Wu, Q. Jiang, X. Song, Y. Chen, L. Cheng, and S. Wu, Fabrication of Dense Zirconia-Toughened Alumina Ceramics through a Stereolithography-Based Additive Manufacturing, *Ceram. Int*., Vol 43 (No. 1), 2017, p 968–972
81. X. Song, Z. Chen, L. Lei, K. Shung, Q. Zhou, and Y. Chen, Piezoelectric Component Fabrication Using Projection-Based Stereolithography of Barium Titanate Ceramic Suspensions, *Rapid Prototyp. J*., Vol 23 (No. 1), 2017, p 44–53
82. Z. Chen, X. Qian, X. Song, Q. Jiang, R. Huang, Y. Yang, R. Li, K. Shung, Y. Chen, and Q. Zhou, Three-Dimensional Printed Piezoelectric Array for Improving Acoustic Field and Spatial Resolution in Medical Ultrasonic Imaging, *Micromachines*, Vol 10 (No. 3), 2019, p 170
83. Y.Z. Ji, Z. Wang, B. Wang, Y. Chen, T. Zhang, L.Q. Chen, X. Song, and L. Chen, Effect of Meso-Scale Geometry on Piezoelectric Performances of Additively Manufactured Flexible Polymer-Pb(Zr_xTi_{1-x})O_3 Composites, *Adv. Eng. Mater*., Vol 19 (No. 6), 2017, p 1600803
84. Y. Yang, Z. Chen, X. Song, B. Zhu, T. Hsiai, P.I. Wu, R. Xiong, J. Shi, Y. Chen, Q. Zhou, and K.K. Shung, Three-Dimensional Printing of High Dielectric Capacitor Using Projection Based Stereolithography Method, *Nano Energy*, Vol 22, 2016, p 414–421
85. J. Luo, L.J. Gilbert, C. Qu, R.G. Landers, D.A. Bristow, and E.C. Kinzel, Additive Manufacturing of Transparent Soda-Lime Glass Using a Filament-Fed Process, *J. Manuf. Sci. Eng*., Vol 139 (No. 6), 2017, p 061006
86. P.T. Brun, C. Inamura, D. Lizardo, et al., The Molten Glass Sewing Machine, *Philos. Trans. R. Soc. (London) A*, Vol 375 (No. 2093), 2017, p 20160156

87. Z.C. Eckel, C. Zhou, J.H. Martin, A.J. Jacobsen, W.B. Carter, and T.A. Schaedler, Additive Manufacturing of Polymer-Derived Ceramics, *Science*, Vol 351 (No. 6268), 2016, p 58–62
88. P. Greil, Polymer Derived Engineering Ceramics, *Adv. Eng. Mater.*, Vol 2 (No. 6), 2000, p 339–348
89. P. Colombo, Engineering Porosity in Polymer-Derived Ceramics, *J. Eur. Ceram. Soc.*, Vol 28 (No. 7), 2008, p 1389–1395
90. E. Zanchetta, M. Cattaldo, G. Franchin, M. Schwentenwein, J. Homa, G. Brusatin, and P. Colombo, Stereolithography of SiOC Ceramic Microcomponents, *Adv. Mater.*, Vol 28 (No. 2), 2016, p 370–376
91. G. Mera, A. Navrotsky, S. Sen, H.J. Kleebe, and R. Riedel, Polymer-Derived SiCN and SiOC Ceramics—Structure and Energetics at the Nanoscale, *J. Mater. Chem. A*, Vol 1 (No. 12), 2013, p 3826–3836
92. J. Bauer, A. Schroer, R. Schwaiger, and O. Kraft, Approaching Theoretical Strength in Glassy Carbon Nanolattices, *Nat. Mater.*, Vol 15 (No. 4), 2016, p 438
93. X. Song, "Slurry Based Stereolithography: A Solid Freeform Fabrication Method of Ceramics and Composites," Doctoral dissertation, Ph.D. thesis, University of Southern California, Los Angeles, CA, 2016